1-1-2005

Conversion of silica diatom frustules to BaTiO3, SrTiO3, and Nb2O5

Shannon Gailene Dudley
Iowa State University

Conversion of silica diatom frustules to $BaTiO_3$, $SrTiO_3$, and Nb_2O_5

by

Shannon Gailene Dudley

A thesis submitted to the graduate faculty

in partial fulfillment of the requirements for the degree of

MASTER OF SCIENCE

Major: Material Science and Engineering

Program of Study Committee:
Mufit Akinc, Major Professor
Keith Woo
Xiaoli Tan

Iowa State University
Ames, Iowa
2005

Graduate College
Iowa State University

This to certify that the master's thesis of

Shannon Gailene Dudley

has met the thesis requirements of Iowa State University

Signatures have been redacted for privacy

1 General Introduction

1.1 Biologically Driven Research

In recent years there has been a large number of interdisciplinary research activities inspired by biology and materials chemistry. For example, researchers have taken inspiration from animal bones which possess enlarged ends to design fiber composites. This structure is used because when the interfacial bonding between the matrix and the fiber is not optimum, composite strengths of fibers with enlarged ends is greater than composites of normal fibers with the same properties and aspect ratios.

In the same area researchers have taken inspiration from tree roots. As an example, riverbanks and dams are often strengthened by planting trees and grasses; their branched roots hold the soil (matrix) in place. Analogous to this application, composites yielded higher strength and fracture toughness when a fractal-tree fiber was used instead of the traditional unbranched fibers. The fibers were formed through vapor growth using benzene as a carbon source, iron as a catalyst, and hydrogen as a carrying gas [1].

The influence of the merger of biology and materials chemistry reaches beyond composite materials. The merger of biology and materials chemistry has worked itself into an extensive variety of materials, especially those with biomedical applications. What could be a better inspiration for biomedical materials than the body itself? For example research is looking into the remarkable way that the body can simultaneously change from one structure or composite to another. Just one example of this is how bone changes from a dense, stiff external structure to a porous internal one without a distinct interface. This continuous change results in optimization of response to external load application. Therefore, researchers are looking at applying the same continuous material change to artificial implants. An example of this is the creation of a functionally graded macro porous hydroxyapatite ceramic. By changing the pore diameter and pore volume fraction though the cross section, the outer layers allowed for cells and blood vessels to access the material and enhance new bone formation while the inner denser ceramic was designed to provide a more mechanically stable implant [2].

Bioinspired research studies the way nature builds structure and develops processing protocols to obtain similar structures in laboratory using non-biological materials while bio-templating actually utilizes natural materials as a template to build structures similar to those in nature. For example, researchers were able to create semiconductor lead selenide nanorods and nanotubes through living bio-membrane bio-templates of mungbean sprouts. Mungbean sprouts were used because they live in solution, and they have special proteins on their biomembranes to transport ions [3]. The researchers deposited PbSe by sequentially dipping the sprouts into $PbCl_2$ and KHSe solutions. Crystal nuclei of PbSe formed and were induced to grow into the morphologies of the templates producing nanorods and nanotubes.

This new cross-over of biology and materials chemistry has produced many exciting research endeavors. It has also provided new ways of looking at material science whether from bio-inspired roots or harnessing nature's abilities through bio-templating. Both bioinspired and biotemplating research has just begun to scratch the surface of this recent combination of biology and materials chemistry and the research presented in this thesis will continue this endeavor.

1.2 Diatoms

Diatoms are single-celled micro-algae that are known to live in various water environments such as the sea, estuaries, fresh water lakes, ponds, streams, ditches, and sometimes in less likely environments like moist rocks, soils, or damp bark [4]. They range in size from 1μm to several millimeters; most in the range between 2-200μm. The internal structures of diatoms include ridges, protuberances, and pores on the order of 100nm [5].

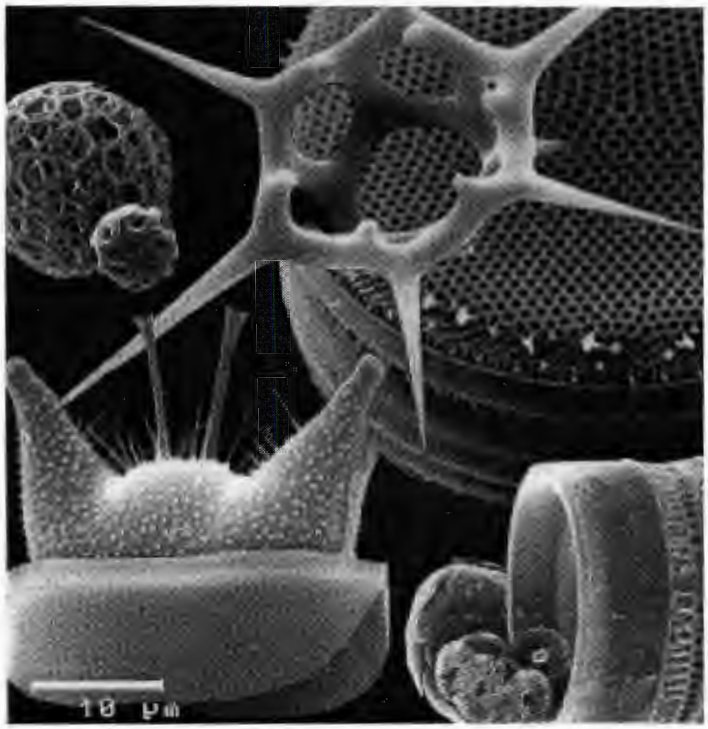

Figure 1 Image demonstrating the different size and shapes produced by different species of diatoms [6]

It is estimated that over 100,000 different species of diatoms exist. Diatoms are classified by their frustule morphologies. Frustules are cell walls which are made mostly of amorphous silica nanoparticles and incompletely characterized organic materials, composed of glycoproteins and carbohydrates [7]. They can form almost any silicified structure [7]. The name "diatom" comes from the fact that they are made of two almost equal halves that fit together like a petri dish [4]. Each half is slightly different. The larger half, the epitheca, fits over the smaller half, the hypotheca. In some species it is very difficult to distinguish between the two halves [5].

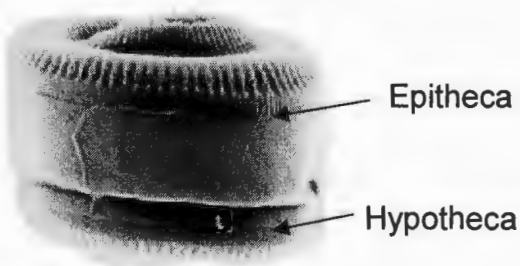

Figure 2 Diatom side view showing the two halves: epitheca and hypotheca[5]

The diatom reproduces asexually by separating the hypotheca and the epitheca which both become epitheca. A new hypotheca is then grown with the help of organelles called the silica-deposition vesicles (SDV). The silica used by the SDV is collected from the environment as silicic acid, which is generally at very low concentrations of <1μM[7]. Asexual reproduction leads to a general decrease in the mean size of the species and an increase in the standard deviation about this mean [4]. The rate of division is a direct effect of the environment but can be as high as eight divisions per day [4]. Once the diatom reaches a terminal size of about 30 to 40% of the maximum diameter of the species, it undergoes sexual reproduction. The resulting offspring is many times larger than both parents and starts to resume rapid asexual reproduction [8].

Once diatoms die they fall to the ocean floor as marine debris. Debris that has a significant amount of diatom frustules is called siliceous oozes, which is usually found in overlying surface waters. After years of siliceous ooze collecting and cementing it forms a rock called diatomite. Sometimes these seafloor rocks become exposed on the land and can be mined. The mined diatomite is used in applications like water filters, abrasives, and pesticides [5].

1.3 Diatom Manipulation

Diatoms have complex three-dimensional structures which are formed in a different way than current manufacturing of silica. Most manufacturing done today is two dimensional and is gravity-based self-assembly, layer-by-layer deposition, or etching. Diatom formation is unlike any industrial based manufacturing technique and is unique in that it is formed without extremes of pH, temperature, and pressure. Harnessing and understanding the unique way diatoms are manufactured could lead to improved industrial processing of silica. It has been proposed that harnessing diatom syntheses and materials chemistry could produce micro/nanodevices that may have applications in biochemical analyses, microsensors, computing and telecommunications, micro-electromechanical or micro-optical devices, microactuators, microfluidic devices, microrobotics, micro fuel cells, and micro batteries. This will require the manipulation of the chemistry and structure of the diatoms. Since the overall morphologies are governed by genetic signatures, wide morphological variety may be

possible by manipulation of the genetic make up of the diatom. It is also possible to non-genetically affect the structure of the diatoms by manipulating the environmental conditions, life cycle stages, or presence or absence of specific chemicals. For example diatoms that are from marine environments have less silica per unit cell volume then diatoms that originate from freshwater. This may be because there is less silicate available in marine environments than fresh water environments. It may also be because of the salinity effect, or because of differences in density of the seawater compared to freshwater. The structure of the diatoms is altered by the degree of silicification. For example, in silicon-limited conditions frustules have structures that are thinner and have larger holes. This means that frustules morphology can be altered by controlling the amount of silica available to the diatom.

Another non-genetic way of modifying the diatom frustules structure is the addition of compounds which include colchicines and amiprophosmethyl (APM) which are microtubule inhibitors or the addition of cytochalasin D which is a actin inhibitor. By adding these compounds the frustules show defects in their well ordered structure. However, these changes are irregular and may result when the inhibitors were added relative to the growth stage of the diatom. Because of the basic irregularity of the changes, adding compounds like these may not be the most useful way of altering frustule composition.

Genetic engineering could allow for greater manipulation and frustule design [9]. Efforts are underway to achieve just this. Recently mapping of the diatom Thalassiosira Pseudonana [10] genome was achieved. This has not shown the exact genes that control cell wall synthesis. In order to achieve this research is underway to identify the genes and proteins that govern the silicification. This may eventually lead to the ability to genetically manipulate the silicified structure [9].

1.4 Gas-solid Reactions [11]

Two well-known examples of gas-solid reactions are the reduction of ores into metal and the combustion of solid fuels. All gas-solid reactions have four main intermediate steps that must be achieved in order to have a successful reaction:

- Diffusion of gaseous reactants to and products from the solid surface
- Diffusion of gaseous reactants or gaseous by products through the pores of solid

- Adsorption of the gaseous reactants on and desorption of the products from the solid surfaces
- The actual chemical reaction between the adsorbed gas and the solid

The first step is the diffusion of the gas reactants to the solid particle, which is controlled by linear molecular diffusion laws. The second step is diffusion of the gaseous reactants through the pores of the solid reaction product or partially reacted solid. In order for the reaction to proceed there has to be a continuous supply of reactants and removal of products. This makes porous diffusion a very important step in gas-solid reactions. However, there are material-specific characteristics that can complicate the diffusion of the gas through the solid. For one, the diffusion path is not a straight line but tortuous and is dependent on the microstructure of the material. For this reason porosity, specific surface area, and pore size distribution of the solid reactant are important characteristics that have a significant role in the rate of the reaction. If pores in the solid are too small, the laws of molecular diffusion can no longer be applied. Knudsen diffusion best demonstrates the diffusion profile. Pressure gradients can also form in the solid, which have to be taken into consideration when trying to control the diffusion of the gas into the solid.

The third step is the adsorption of the gaseous reactants on the surface of the solids as well as the desorption of the byproducts away from the surface. The nature of the adsorption onto the surface of the bulk materials is very specific to the materials in question. In general, the surface of the bulk material, when in contact with gas, will have a finite amount of adsorption.

There are two main types of adsorption, physical absorption and chemisorption. Physical adsorption is the weaker of the two types. In physical adsorption molecules are attracted to the surface atoms through van der Waals or dispersion forces. These forces are known to be long-range and as a result can lead to many layers of adsorbed species. If adsorption continues, it can lead to condensation of a liquid (and even solid) phase. Physical adsorption will also be similar on different surfaces under similar conditions because of its similarity to condensation, i.e. non-specific attraction. Like condensation, physical adsorption requires very little activation energy to occur.

Chemisorption has much stronger interaction forces than physical adsorption, approximating those of chemical bonds. However these valence forces do not have the same long-range interaction. Chemisorption is limited to a monolayer coverage. Chemisorption is unique to the gas and the solid in consideration. They must be compatible in chemical forces and orientation for chemisorption to proceed, i.e. they are site specific. Chemisorption in general requires higher activation energy, which generally means that its reaction rate is lower than that of physical adsorption.

Physical adsorption is most significant at temperature ranges below the boiling point of the adsorbate, while chemisorption is most significant at higher temperatures. All these factors play just as important a role in desorption of the product gas as they do on the adsorption of the reactant gas. Without desorption of the product, the surface of the solid is not available for further reaction.

The final step in gas-solid reactions is the actual chemical reaction between the adsorbed species and that of the solid. The probability of a spontaneous reaction taking place under a given set of experimental conditions can be estimated from free energy of the specific reaction under consideration. After the surface has reacted to form a product layer around the particle, solid diffusion has to occur through the solid to have full conversion. In order for this to occur, the gaseous reactant must penetrate through the product layer in order for the reaction to go to completion.

Figure 3 shows the schematic representation of a sold-gas reaction which consists of chemical reactions at the interface and the diffusion of the gaseous reactants and products through the solid product layer

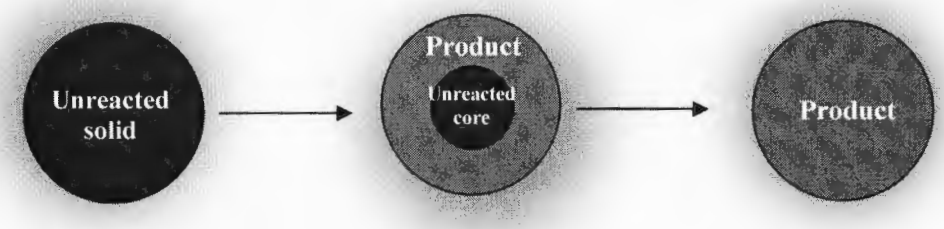

Figure 3 Gas-solid reaction proceeding with the formation of a shrinking unreacted core

1.5 Sensors

1.5.1 Introduction

Sensitivity of semiconductive metal oxides to the gas composition of the surrounding atmosphere was first noted in 1962 [12]. Later that year, ZnO and porous SnO_2 were demonstrated as effecti ve gas-sensing devices. Soon after, Figaro Engineering Inc. developed the first porous SnO_2 pellet for application as a commercial sensor for domestic gas leaks. This sensor was modified for other gas detection like CO and H_2S. The next major milestone in the history of gas sensors was the introduction of the first TiO_2 oxygen sensor by NGK Spark Plug Co. Ltd. This sensor was used to control the air/fuel ratio in automobile engines. Some of the main metallic oxides being researched today are SnO_2, TiO_2, FeO_3 and WO_3. There have been many attempts to improve the sensitivity, selectivity and stability of these metal oxide gas sensors. Some of the driving forces for these advances in sensor technology are increasing concern over domestic and industrial safety, finer control over manufacturing processing steps, and legislative actions governing harmful gaseous emissions from stationary and mobile sources[13]. Advances in sensor performance have been realized by changing preparation methods, introducing minor elements, and forming electron donor and acceptors on the surface [14, 15].

One of the ways to greatly increase the sensitivity and response of sensors is through use of nano-crystalline materials. It has been proven that gas-sensing properties can be

improved by grain-size reduction and gas-diffusion control [16]. As the crystallite size of metal oxides decreases, the contribution of the surface energy to total free energy of the system greatly increases. The increase in surface area results in a high activity of the material. It is for these reasons that nano-crystalline semi conducting oxides are very promising in the development of high-sensitivity fast-response gas sensors [17].

1.5.2 Sensing Mechanism

Ceramic sensors are superior to other materials as sensors for their high mechanical strength, chemical resistance, and increased thermal stability. Semiconducting oxide sensors respond by their resistivity changes in response to different concentrations of atmospheric gases. Several kinds of oxygen adsorbates are known to cover the surface of semi-conductive metal oxides in air; they include O_2^-, O^-, and O^{2-}, O^- are the most reactive species with inflammable gases. The surface coverage of O^- eventually leads to a dominating factor in sensor resistance. In n-type semiconductive metal oxides, space-charge regions form on the surface of the grains. Due to the transfer of electrons from the grain surfaces to the adsorbates, this results in an electron-depleted surface layer.

$$O_{2(g)} + 2e^- = 2O^-$$

The depth of the space-charge layer is a function of the electron concentration in the bulk as well as the surface coverage of adsorbed oxygen. Each grain boundary creates a potential barrier to electronic conduction which results in a high resistance in n-type semiconductor gas sensors. However, when the same sensor is exposed at high temperatures to an atmosphere of flammable gases the adsorbed oxygen is consumed. This lowers the steady-state surface coverage of the adsorbates. As a result, the electrons fixed by the adsorbed oxygen adsorbates go back to the oxide grains bulk material which causes the potential barrier to drop and the resistance to decrease. Figure 4 shows the schematic representation of space charge layer and associated potential drop with change in oxygen coverage on the surface.

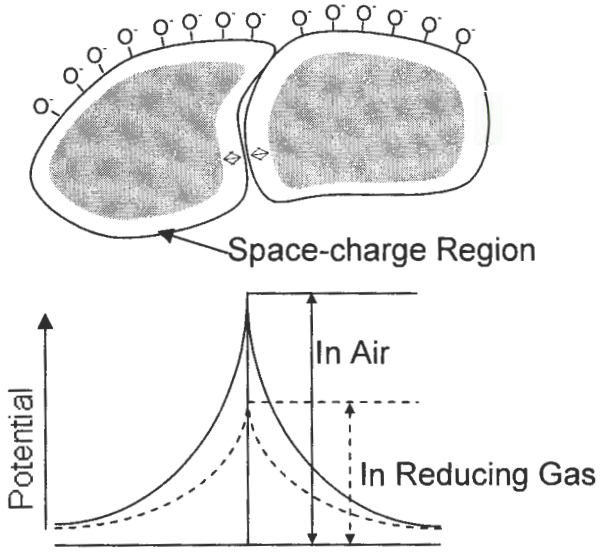

Figure 4. Potential barrier to electron conduction at grain boundary in n-type semicondutive metal oxides

Sensitivity of the gas sensor is defined as the ratio between the resistances in air to that of the sample gas containing an flammable component. Selectivity is often a problem with semiconducting gas sensors because the sensors respond to many gases. This can result in cross sensitivity, which is the inability to select a specific gas to measure. In oxidizing gases like CO and NO_2 the sensor's resistivity increases. This is a result of their negatively charged chemisorption on the grain surface. Sensitivity then becomes a function of the amount of chemisorption on the surface.

P-type semiconductive metal oxides are the opposite of n-type semiconductive metal oxides. In air the resistance is low because of the formation of negatively charged oxygen adsorbates which results in the removal of electrons from the bulk creating more holes in the grain surface. In flammable gas atmospheres the consumption of oxygen adsorbates causes an increase in resistance [13].

1.5.3 Grain Size Effects

Two of the most important factors that affect the sensitivity of semiconductive metal oxide gas sensors is the actual grain size or crystallite size, D, and the space-charge depth, L. To illustrate the effect of grain size on the sensitivity of gas sensors an example of pure

SnO_2, a popular semiconducting oxide gas sensor, is used. Figure 5 shows the sensitivity of the SnO_2 sensor vs. its grain size [12]. It can be observed that as the crystallite size decreases the sensitivity greatly increases. This is due to the space-charge region of the grain gradually taking over the entire grain resulting in a higher sensitivity. It was measured that in thin films of SnO_2 the space-charge region was about 3nm thick. Since the grains can be roughly estimated to be spheres the critical size of space-charge consumption would be around 6nm or 2L. As the crystallite size decreases even further, the sensitivity still increases because of the increase in the amount of oxygen adsorbed per volume which is directly related to the surface area. The sensitivity in the figure is defined as R_a/R_g were R_a is the electric resistance of the elements in dry air and R_g is the resistance in 800 ppm H_2-dry air mixture [12].

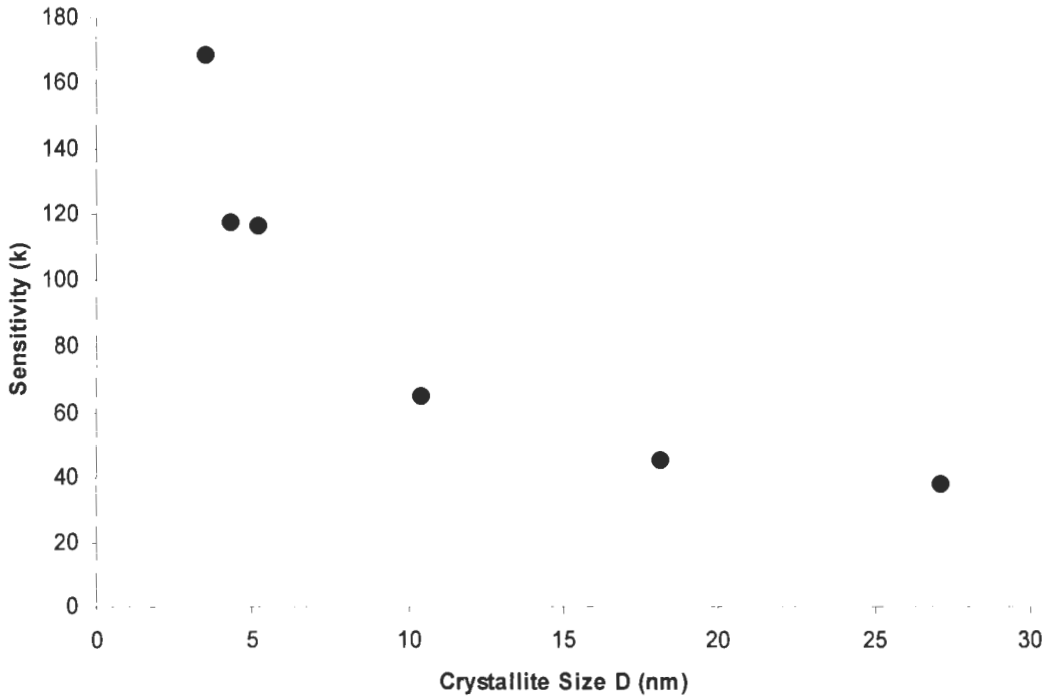

Figure 5 SnO_2 sensors sensitivity to 800 ppm H_2 as a function of crystallite size D

1.5.4 Nb Doped TiO_2 Sensors

TiO_2 is one of the most popular choices of sensor materials in gas detection. TiO_2 sensors have a high resistance to Pb when immersed in gasoline which makes them an excellent choice to be used in Air/Fuel ratio control in automobile engines [15]. TiO_2 is being researched in a wide range of applications including sensing for NO_x, NO_2, CO, and CO_2.

Sensing capacity of TiO_2 is increased by doping with elements like Pt, Cu, Cr, and Nb. It has also been documented that impurity ions of valency greater than four, like Nb^{+5}, reduces the oxygen vacancy concentration and inhibits the transformation of anatase titania into rutile titania [18]. Addition of Nb to TiO_2 has also been extensively studied for oxygen sensing. Nb addition creates a higher sensitivity at lower working temperatures. There have also been studies illustrating the possibility of using Nb-doped TiO_2 sensors for CO or alcohol monitoring. A general description of how Nb doping effects TiO_2 performance is that it modifies the microstructure of the base material, controls grain growth mechanisms, and introduces electronic states at the surface or in the bulk of the grain which change the base conductivity and the gas sensing properties. Introducing niobium into titania may increase the concentration of electrons as well as induce the creation of a donor level by the formation of defects which include vacancies or interstitial oxygens. This shifts the Fermi level toward a location closer to the conduction band [19], which reduces the electrical resistance of TiO_2 but still maintains its n-type behavior unlike other dopants such as chromium, which changes the conductivity of titania to p-type [20].

1.5.5 Nb_2O_5

Although the automotive industry is the largest consumer for oxygen sensors, there is a great need for oxygen sensors in different applications including but not limited to mines, incubators in hospitals, and combustion control in large sized furnaces. Since applications require different requirements in sensing whether it is in a lean or rich oxygen environment or what temperature range of operation is expected, different sensors for different applications must be developed. Nb_2O_5 sensors have been used in ceramic kiln applications. Nb_2O_5 sensors were tested in the range of 10 ppm to 100% oxygen partial pressure and at temperatures betweeen 400 and 800°C. Nb_2O_5 sensors showed excellent sensitivity toward oxygen in the temperature range 400-800°C with reasonable response time and good reversibility upon exposure to increasing and decreasing oxygen partial pressures [21]. Other studies into the gas sensing application of Nb_2O_5 have shown that it could be used for sensing petroleum constituents after calcining at 900-1000°C and that it has good selectivity for C_2H_5OH, H_2, and i-C_4H_{10} [22].

1.5.6 $BaTiO_3$ and $SrTiO_3$

$BaTiO_3$ is the most investigated ferroelectric material mainly because of its simple structure. $BaTiO_3$ shows ferroelectric properties at and above room temperature, and it is easy to prepare and use. $BaTiO_3$ has a curie temperature of 120°C and a perovskite-type structure. The structure belongs to a family of ABO_3 compounds including $CaTiO_3$ and $SrTiO_3$. Above 120°C, $BaTiO_3$ is cubic with a m3m point group. From 5°C to 120°C, $BaTiO_3$ is tetragonal with a 4mm point group. In order for the cubic $BaTiO_3$ to distort to the tetragonal $BaTiO_3$ on cooling, one of the cube edges elongates and becomes the tetragonal *c* axis while the other edges compress and become the *a* axes. A schematic showing how the unit cell changes with the transition from tetragonal to cubic is shown in Figure 6. Because the shift is asymmetric, the overall center of positive charge is separated form the overall center of negative charge producing a permanent electrical dipole in the tetragonal $BaTiO_3$ [23].

$BaTiO_3$ posses two phases in addition to the two already discussed. Rhombohedral phase is stable below -90°C. Between -90°C and 5°C an orthorhombic phase is stable. However, the cubic and tetragonal phases, along with their associated transition, are the most relevant for most application purposes.

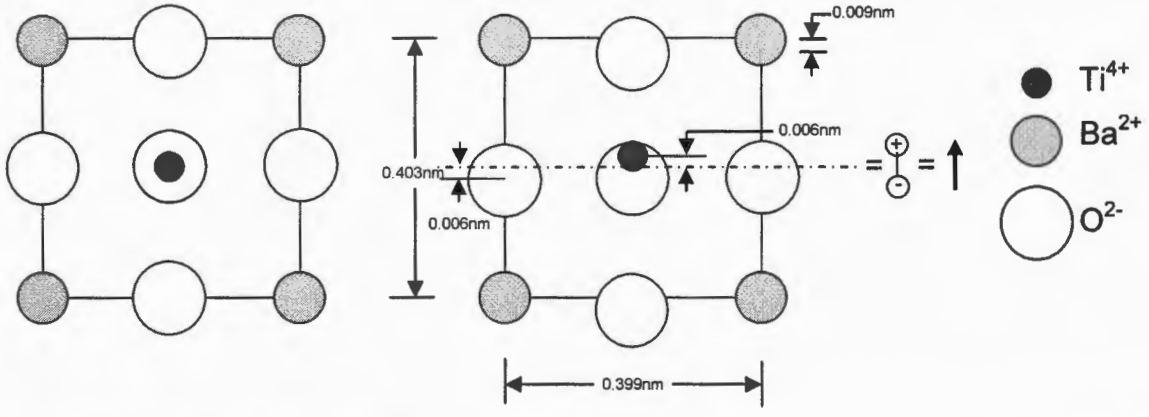

Figure 6 shows the front view of cubic $BaTiO_3$ and that of the tetragonal structure. The figure shows the electrical dipole formed during the tetragonal phase. Note: The scale of the ions and there shifts have been exaggerated [24].

$SrTiO_3$ is a well known ferroelectric and piezoelectric material with many of the same properties of $BaTiO_3$ including a perovskite structure. One thing that separates $SrTiO_3$ from

$BaTiO_3$ is their cubic-tetragonal phase transitions. $SrTiO_3$ has a phase transition well below room temperature (105K [25]). As a result $BaTiO_3$ is more popular but $SrTiO_3$ is a useful material and does have some of the same applications of that $BaTiO_3$ [26].

1.6 Displacement Reactions

1.6.1 Introduction

Because of their relevance to the present work, only the displacement will be discussed in here: single displacement reactions, and double displacement reactions.

A single displacement reaction occurs when a new atom or ion replaces an existing atom or ion of a compound. An example of a common displacement reaction is the displacement of copper in copper sulfate by zinc to form zinc sulfate in the following reaction:

$$Zn(s) + CuSO_4(aq) \rightarrow Cu(s) + ZnSO_4(aq)$$

A double displacement reaction occurs when species from two compounds displace each other and form new compounds. Double displacement reactions may occur when one of the products is removed from the solution as a gas or precipitate or when the two species combine to form a weak electrolyte that remains associated in solution. An example of double displacement is the reaction between calcium chloride and silver nitrate which forms a silver chloride precipitate in a solution of calcium nitrate [27].

$$CaCl_2(aq) + 2AgNO_3(aq) \rightarrow Ca(NO_3)_2(aq) + 2AgCl(s)$$

A specific type of displacement reaction is the shape preserving displacement reaction. This reaction can be a single or double displacement reaction where the solid reactants shape is preserved even after the reaction is completed.

1.6.2 Shape Preserving Displacement Reactions

An example of shape-preserving displacement reactions was performed by Breslin *et al.* [28]. This reaction was the creation of a near net shape composite of Al_2O_3 and Al from an original SiO_2 template by the use of a liquid phase displacement reaction. This was achieved by submersion of SiO_2 preforms made from rods of fused quartz glass or a slip cast

of fused SiO_2 powders in a molten liquid Al bath between 700°C and 1300°C. Under these conditions the following reaction occurred.

$$3SiO_2(s) + 4Al(l) \rightarrow 2Al_2O_3(s) + 3[Si]_{Al}$$

In the above reaction $[Si]_{Al}$ represents the diffusion of silicon out of the preform and into the surrounding liquid aluminum bath. The result was an interpenetrating continuous phases of Al and Al_2O_3, with the same net shape of the original preform and ~1% linear change.

Wagner *et al.* [29] also used performs of TiO_2 and Al_2O_3 that were sintered at 1250°C and then placed in a crucible and embedded in aluminum chips. The crucible was then heated to 850°C and placed under 12MPa argon pressure. This resulted in the infiltration of molten Al into the perform and the following reaction occurred.

$$3TiO_2(s) + 13Al(l) \rightarrow 2Al_2O_3(s) + 3TiAl_3(s)$$

The result was a near net shape process that produced an $Al_2O_3/TiAl_3$ composite.

Binnewies *et al.* [30] used shape preserving displacement reactions in the formation of FeSi from Fe with the following reaction.

$$3Fe(s) + SiCl_4(g) \rightarrow FeSi(s) + 2FeCl_2(g)$$

This reaction was different from its predecessors in that it used a gas-solid reaction instead of a liquid solid reaction. In the reaction an iron spring was exposed to $SiCl_4$ gas at temperatures around 1000°C for times up to 3 hours. The final product was FeSi with no shape change. This was surprising as there was a calculated 34.5% volume loss with reaction. The volume loss was offset by the formation of a porous FeSi. The porous nature also facilitated the diffusion of the product and reactant gases in and out of the solid.

Sandhage *et al.* [31] like Binnewies used a shape preserving gas-solid displacement reaction. Sandhage and his coworkers used diatom frustules with a solid meso-scaled amorphous silica template and converted the amorphous silica into MgO. Exposing the frustules to magnesium at 900°C for 4 hours accomplished this. At 900°C magnesium is molten with a significant vapor pressure, which underwent the following reaction

$$2Mg\ (g) + SiO_2 \rightarrow 2MgO\ (s) + \{Si\}$$

Where the {Si} refers to silicon dissolved within Mg-Si liquid. The end result was the shape preservation of the frustules. Kalem [32] reproduced this work in our laboratory.

Sandhage *et al.* also predicted other possible shape preserving displacement reactions that could be used to generate other compositions.

$$\tfrac{4}{3}\,AlF_3(g) + SiO_2(s) \rightarrow \tfrac{2}{3}\,Al_2O_3(s) + SiF_4(g)$$
$$2Ca(g) + SiO_2(s) \rightarrow 2CaO(s) + \{Si\}$$
$$\tfrac{4}{3}\,FeF_3(g) + SiO_2(s) \rightarrow \tfrac{2}{3}\,Fe_2O_3(s) + SiF_4(g)$$
$$4Li(g) + SiO_2(s) \rightarrow 2Li_2O(s) + \{Si\}$$
$$\tfrac{4}{5}\,NbF_5(g) + SiO_2(s) \rightarrow \tfrac{2}{5}\,Nb_2O_5(s) + SiF_4(g)$$
$$2Sr(g) + SiO_2(s) \rightarrow 2SrO(s) + \{Si\}$$
$$\tfrac{4}{5}\,TaF_5(g) + SiO_2(s) \rightarrow \tfrac{2}{5}\,Ta_2O_5(s) + SiF_4(g)$$
$$TiF_4(g) + SiO_2(s) \rightarrow TiO_2(s) + SiF_4(g)$$
$$ZrF_4(g) + SiO_2(s) \rightarrow SiF_4(g) + ZrO_2(s)$$

Sandhage *et al.* [33] also continued his work with the formation of titania (TiO_2) using the same frustules as preforms. The present work was undertaken using the following equation previously proposed [31].

$$TiF_4(g) + SiO_2(s) \rightarrow TiO_2(s) + SiF_4(g)$$

The above reaction differed from the previous reaction by the use of a double displacement reaction instead of a single displacement reaction. The use of TiF_4 provided a suitable gaseous reactant at a moderate temperature and displacement results in formation of a gaseous SiF_4 by-product. This allows easy removal of by-products from the system. This reaction was done in a sealed titanium reactor where the TiF_4 and frustules were heated to 350-700°C for 2 hours. However, EDS showed significant concentrations of titanium, fluorine, and oxygen. This was explained by three possible reactions.

$$TiF_4(g) + \tfrac{1}{2}\,SiO_2(s) \rightarrow TiOF_2(s) + \tfrac{1}{2}\,SiF_4(g)$$
$$TiF_4(g) + \tfrac{2}{3}\,SiO_2(s) \rightarrow TiOF_2(s) + \tfrac{1}{3}\,Si_2OF_6(g)$$
$$TiF_4(g) + SiO_2(s) \rightarrow TiOF_2(s) + SiOF_2(g)$$

In order to form anatase the frustules were reheated to 350°C for 2 hours while exposed to oxygen.

$$TiOF_2(s) + \tfrac{1}{2}\,O_2(g) \rightarrow TiO_2(s) + F_2(g) \qquad \Delta G°(350°C) = 68.2 \text{ KJ/mol}$$

However, the probability of forming $F_2(g)$ is very unlikely because of thermodynamically it is not favored at the temperature. A plausible reaction that was not considered is: $TiOF_2 + H_2O(g) \rightarrow TiO_2(s) + 2HF(g)$ $\Delta G°(600°C) = -257.2$ KJ/mol

Nevertheless, the final product was anatase with a fine oxide crystal structure with a grain size less than 100nm and the frustule morphology was claimed to be preserved. Examination of the micrographs does support the retention of frustule morphology.

Conversion of silica frustules to other oxides including titania was simultaneously carried out by Kalem and Akinc [32] with a slightly altered procedure. Kalem and Akinc employed a stainless steel reactor instead of titanium and reaction was carried at lower temperatures than those by Sandhage et al. They also performed the conversion of $TiOF_2$ to TiO_2 in an air atmosphere instead of oxygen. In the end, the same net shape was persevered and the SiO_2 frustule was converted to anatase.

Kalem also attempted conversion of anatase to $BaTiO_3$ by reacting TiO_2 with $Ba(OH)_2 \bullet 8H_2O$ according to following reaction:

$$Ba(OH)_2 \bullet 8H_2O(l) + TiO_2(s) \rightarrow BaTiO_3(s) + 9H_2O(l)$$

$$TiO_2(s) + PbO(l) \rightarrow PbTiO_3(s)$$

After the reaction the excess $Ba(OH)_2$ was removed by dissolving in water and removing from the anatase frustules with filtration. Akinc and Kalem predicted that $SrTiO_3$ or $PbTiO_3$ could be synthesized using similar reactions with strontium hydroxide and lead oxide as reactants.

$$TiO_2(s) + Sr(OH)_2(l) \rightarrow SrTiO_3(s) + H_2O(g)$$

1.7 Conversion Requirements

There are four distinct requirements for a successful gas-solid shape preserving displacement reaction. Each one must be met in order to have a successful reaction. They are: thermodynamic favorability, volume conservation, practicality of reaction conditions, and ease of separation of byproducts. The first, thermodynamic favorablity, means the reaction must have an overall negative ΔG of reaction. All proposed reactions must be checked to see if the reaction is indeed thermodynamically favorable. The second requirement needs to be taken into consideration is conservation of volume. In order to have successful shape preservation, the volume change should be small enough to maintain the original shape of the frustule. The limit for volume change that the frustule shape can be retain has not been

established. The third requirement is reasonable reaction conditions leading to conversion. All conversion reactions must be achievable under practical time, temperature, and atmosphere combinations. To be practical at the industrial scale, conversions also have to be repeatable. The fourth requirement is the ease of separation of byproducts. This is an important requirement in order to have desired solid product without contamination of other elements. For example, if the silica frustule is converted to another metal oxide, it is desirable to remove the silicon as a gaseous byproduct. Gaseous by-products are by far the most desirable because they can be easily vented out of the system. Water soluble by-products are also desirable. This allows removal of the unwanted byproduct by washing and/or filtering. These four are necessary in order to have a successful shape-preserving reaction.

There is more then one approach to the convert silica frustules to other materials. One approach is to use gas solid displacement reaction which removes the silicon and replaces it with a metal of choice. However this process is always performed at elevated temperatures with perished diatoms. Another approach being investigated is to see if the material conversion could be done during the development of the diatom. Instead of the diatom removing $Si(OH)_4$ from the environment and converting it to hydrated SiO_2, research is being conducted to see whether diatoms can process other metals similar to silicon, e.g. germanium [34]. Silicon-germanium oxide composites are reported to have semicoducting and optoelectronic properties with potential applications in fabrication of microelectronic devices. In order to make this possible a two-stage photobioreactor cultivation process was developed. In the first stage, the diatoms were cultivated in a $Si(OH)_4$ solution until the diatoms consumed $Si(OH)_4$ to a point of silicon starvation. In stage two, the Si-starved diatoms were fed either $Ge(OH)_4$ or a mixture of $Ge(OH)_4$ and $Si(OH)_4$. In both solutions the diatoms rapidly assimilated both the $Ge(OH)_4$ and $Si(OH)_4$. However when only $Ge(OH)_4$ was added diatoms did not divide. In the mixture of $Ge(OH)_4$ and $Si(OH)_4$ cell division continued but at a slower rate when compared to only adding $Si(OH)_4$. Characterization of the thermally annealed diatoms showed that they were indeed nano-granular with features ranging from 20-100nm that were made of SiO_2-GeO_2 composite with some addition of calcium which was inadvertently added during the second stage of the reaction. The particles were amorphous before annealing, but crystallized during annealing.

This research shows that the conversion of diatom frustules to different materials is being attempted in many different ways and each has its limitation. This particular conversion is limited by the element selection and may not be suitable to other elements that are not similar to silicon. But unlike the germanium reaction, in the shape preserving displacement reactions the diatoms are not alive and reactions are carried at elevated temperatures. Each reaction has its advantages and disadvantages which may prove to be useful for different applications.

2 Conversion of Silica Frustules to TiO_2, $BaTiO_3$, and $SrTiO_3$

Shannon Dudley and Mufit Akinc

Department of Materials Science & Engineering

Iowa State University, Ames, Iowa 50011

Abstract

Diatom frustules were used as bio-templates to synthesize functional ceramics via solid-gas displacement reactions. Silica based frustules were exposed to TiF_4 at 330°C to form $TiOF_2$ which is later converted to TiO_2 (anatase) by heat treatment in air at 600°C. The TiO_2 frustules were then exposed to $Ba(OH)_2$ at 120°C or $Sr(OH)_2$ at 160°C to form $BaTiO_3$ or $SrTiO_3$ respectively. Chemical composition, structure, and morphology of the converted frustules were studied by XRD, TEM, SEM, EDS. In both cases near complete conversion was achieved while retaining the morphology of the original silica frustules.

2.1 Introduction

The world is on the edge of a nanotechnology revolution [1], and its effects are starting to work their way into our everyday lives in every shape and form. This is causing a lot of research focus to switch from "Can we do it?" to "Can we make it affordable?", and this question is making researchers look at completely new ways of manufacturing. As a result researchers are looking to the ultimate manufacturing plant "nature" as their inspiration. This in turn, has created a whole new area of study referred to as bio-inspired processing and bio-templating science.

Nature has the ability to synthesize nanostructured composite materials and direct their assembly into elaborate microstructures that are simple to manufacture, scaleable, and environmentally friendly in the form of diatoms [2]. Diatoms are single celled micro algae made primarily of amorphous silica nanoparticles. It is estimated that over 100,000 different species of diatoms exist [3]. Diatoms are classified by their frustule morphologies. Frustules are cell walls which are made of mostly amorphous silica nanoparticles [3]. By harnessing nature's ability to create these complex shapes and maybe some day even using genetic

engineering to control the diatom design [4] it may be possible to change the way micro manufacturing is done. Efforts are already underway to understand how diatoms manufacture themselves with the finished mapping of the diatom *Thalassiosira Pseudonana* genome [5]. However, that still leaves the challenge of controlling the composition of the frustules.

Silica has limited properties but by changing the frustule composition to more useful materials like TiO_2, $BaTiO_3$, and $SrTiO_3$, the applications of such frustules exponentially grows. In order to achieve this, this paper reports several different shape preserving reaction schemes to convert diatoms into different materials like TiO_2, $BaTiO_3$, and $SrTiO_3$.

TiO_2 is one of the most popular choices in gas detection. TiO_2 sensors have a high resistance to lead when dissolved in gasoline which makes it an excellent choice to be used in Air/Fuel ratio control in automobile engines [6]. TiO_2 is being considered for a wide range of applications including NO_x, NO_2, CO, and CO_2.

$BaTiO_3$ is found in a wide range of applications in electronic systems because of its excellent electric and electromechanical properties [7], but most notably as a ferroelectric and piezoelectric material. It is recognized to have a high dielectric constant and resistivity. These properties make $BaTiO_3$ a useful material in many applications including multilayer capacitors, electro-optical devices, thermistors, piezoelectric actuators, nonlinear resistors, thermal switches, passive memory storage devices, and transducers. It has also been used in chemical sensors because of its sensitivity to gas adsorption [8,7] Main interest in $BaTiO_3$ stems from its ferroelectric properties at ambient temperature. $BaTiO_3$ has a reported curie temperature of around 120°C; transforming tetragonal to cubic upon heating [9]. Synthesis of $BaTiO_3$ can be achieved in a variety of ways which include solid-state reaction, coprecipitation, sol-gel method, hydrothermal method, and precipitation in inverse micro-emulsion [10]. The hydrothermal method has two different approaches for conversion. One of the approaches involves reaction of soluble Ba^{2+} with hydrated oxy titanium complexes to precipitate $BaTiO_3$. In this mechanism the $BaTiO_3$ are inherently different in size and morphology than their precursor TiO_2 particles, and therefore this is not a viable method for shape preserving reactions. The second method is a viable candidate for shape preserving reaction and is used in this work. In this method, Ba^{2+} ions in aqueous solution react with TiO_2 to form a $BaTiO_3$ shell around a TiO_2 core. Presumably, the Ba^{2+} ions then diffuse

though the shell and react with the core TiO_2, and full conversion to $BaTiO_3$ (or some hydrated form) is achieved. The rate determining step of this mechanism can be either the diffusion through the particle or the reaction at the $BaTiO_3/TiO_2$ interface [10]. At high Ba^{2+} concentrations, the diffusion through the $BaTiO_3$ product layer is fast so that the rate determining step is the reaction of Ba^{2+} with TiO_2 at the interface. When the Ba^{2+} concentration is low, the transportation rate to the interface is slow so the interface is no longer saturated Ba^{2+} and the diffusion of Ba^{2+} though the $BaTiO_3$ product layer becomes the rate determining step [11].

$SrTiO_3$ is also a well-known ferroelectric and piezoelectric material. It has a perovskite structure but has a tetragonal-to-cubic-phase transition at -169°C [12]. Because of this, $SrTiO_3$ is often used in similar applications as $BaTiO_3$ but at lower temperatures [13]. Synthesis of $SrTiO_3$ can also be achieved by many of the same methods as used for $BaTiO_3$ including the hydrothermal method [14] which is the method of choice for the work reported here.

In order to convert the silica frustules to other materials, four key requirements need to be met. The first is the reaction has to be thermodynamically favorable (i.e. $\Delta G^{o}_{R} < 0$). Without this, the reaction will not continue in the direction that is desired. The second requirement is the conservation of volume. This means that as the materials change from SiO_2 to any other material the change in molar volume has to be small enough not to cause to much strain in the system to preserve the diatom's original shape. The third requirement is that the reaction conditions should be practical and robust to be reproducible. And the final requirement is the ease of separation of byproducts of the reaction. This requirement makes gas-solid displacement reaction an excellent choice for product separation and shape preservation. Ingas-solid displacement reaction, the gas diffuses to the reactant surface where it diffuses though pores of the solid and is adsorbed on the solid surface where the actual chemical reaction between the gas and the solid occurs. After the chemical reaction, the byproduct gas has to desorbed from the solid surface and diffuse out of the product layer though the pores of the solid. For example, the conversion of SiO_2 frustules to MgO oxide was achieved by the following reaction [15].

$$2Mg(g) + SiO_2(s) \rightarrow 2MgO(s) + Si(s) \qquad \Delta G_{900C\ Pmg=0.16atm} = -245.2\ kJ/mol$$

The byproduct is Si(s) which is not easily removed from the desired MgO frustule. In the ideal reaction the byproduct would be a gas that should be vented away or a material that could be easily removed such as a water soluble byproduct.

Previous work by Sandhage and coworkers successfully converted the silica frustules to MgO [15] according to the equation above and later to TiO_2 [16] under the following reaction.

$$TiF_{4(g)} + SiO_{2(s)} \rightarrow TiO_{2(s)} + SiF_{4(g)}$$

Sandhage also reported the intermediate structure of $TiOF_2$ in which he removed by reheating the $TiOF_2$ in O_2 to 350°C for 2 hours. For conversion to TiO_2, they reacted the intermediate $TiOF_2$ with oxygen and they claimed it it formed TiO_2 and F_2(g) according to:

$$TiOF_{2(g)} + O_{2(g)} \rightarrow TiO_{2(s)} + F_{2(g)}$$

However, this does not seem to be the reaction path as formation of molecular fluorine gas, F_2 is not thermodynamically favorable in this reaction.

The conversion to MgO was reproduced by Kalem and later the conversion of silica frustules to TiO_2 was simultaneously being developed [17]. Like Sandhage, Kalem reacted silica frustules with TiF_4 to produce $TiOF_2$. However Kalem heated the $TiOF_2$ to 600°C in air where it was believed to under go the following reaction:

$$TiOF_2 + H_2O(g) \rightarrow TiO_2(s) + 2HF(g) \quad \Delta G°(600°C) = -257.2 \text{ kJ/mole}$$

The present work examines the conversion of silica frustules to TiO_2 in more detail using the procedure developed by Kalem and will continue the conversion to form $BaTiO_3$ and $SrTiO_3$ using the shape preserving hydrothermal method. In this conversion, the silica frustules will be first converted to TiO_2 and then exposed to $Ba(OH)_2$ and $Sr(OH)_2$ were they will be converted to $BaTiO_3$ and $SrTiO_3$ at elevated temperatures. This will result in $BaTiO_3$ and $SrTiO_3$ particles that retain many of the features and morphology of the silica precursors.

2.2 Materials and Methods

Commercially available diatomaceous earth was used as a source of frustules in this study and were purchased from Glorious Gardens, Inc. (Des Moines, IA). Prior to chemical conversion operations, residual organic material is removed by heating the diatomaceous

earth in a crucible furnace at 600°C for 8 hours. Once the organic contaminants were removed, the diatomaceous earth sample was subjected to sedimentation in water to eliminate broken pieces and fine debris. The settling process involved placing approximately 15 g of pyrolyzed sample in a one-liter plastic bottle, which was filled with de-ionized water and shaken until the frustules were fully dispersed. The frustules were then allowed to settle for 2 hours, the supernatant was poured off, and the process was repeated five times. The frustules were then transferred to a petri dish and dried in an oven at 98°C overnight. The dried sample was collected and kept in a sealed container for use in all conversion reactions (See Figure 1).

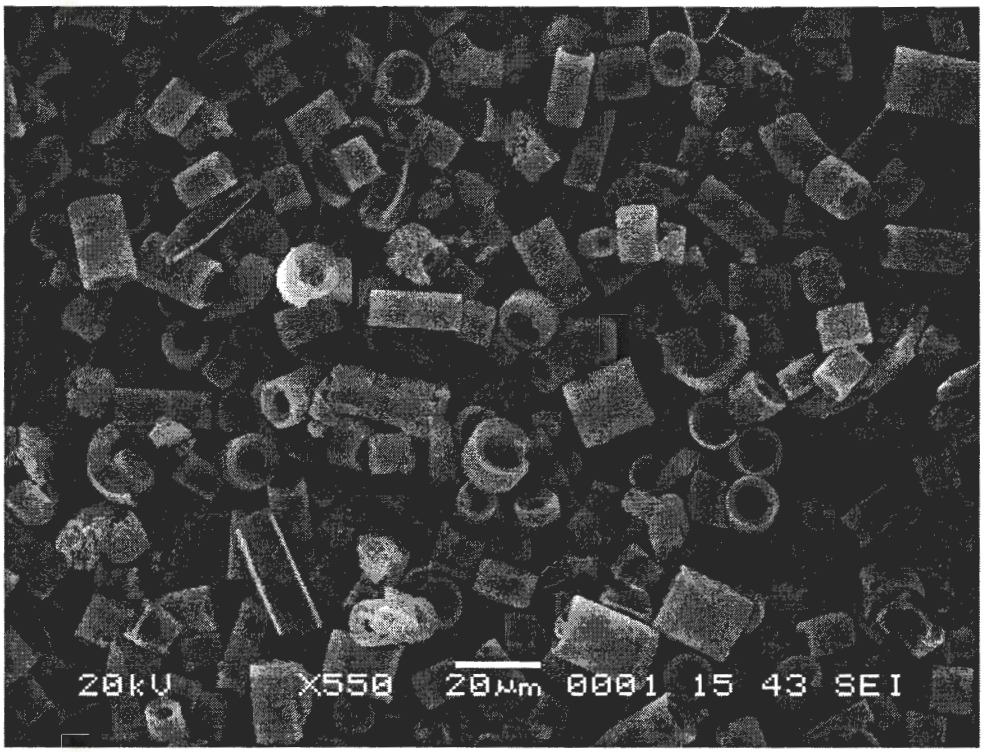

Figure 1. SEM of silica frustules after organic matter removal by pyrolysis and separating from debris by sedimentation. Note most of the frustules are intact and free from debris. Dimension of typical frustule is about 10 to 30 µm in length. Also note that most of the frustules have the same general morphology and fine features.

Conversion of SiO_2 frustules to TiO_2 was attempted by placing 0.87g TiF_4 granules (Alfa Aesar, 98% pure) in one of the two reactant cavities of the stainless steel reactor. 0.17g pyrolyzed silica frustules were placed in the other cavity. The reactor was sealed in an argon atmosphere in order to prevent moisture from reacting with the hygroscopic TiF_4 and to

avoid any contamination of the reactants with carbon dioxide. Figure 2 schematic drawing of the stainless steel reactor.

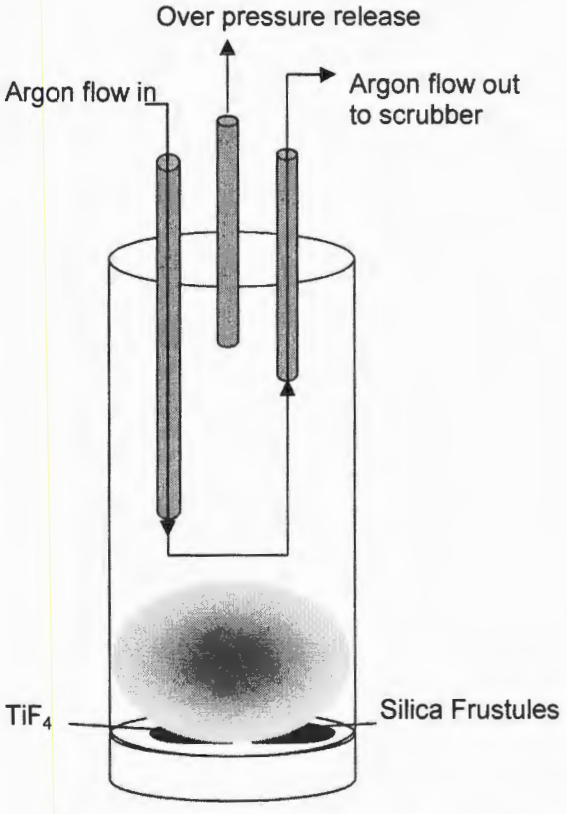

$$TiF_4(g)+\tfrac{1}{2}SiO_2(s)\rightarrow TiOF_2(s)+\tfrac{1}{2}SiF_4(g)$$

Figure 2 Diagram of stainless steal reactor

Once the reactor was sealed it was placed in a crucible furnace that was heated to 330°C at a rate of 5°C/min and held at this temperature for 90 minutes before cooling to room temperature. In the last 30 minutes of the soak time, the reactor was purged with argon at a rate of 20 mL/minute, until the reactor had cooled well below the sublimation temperature of the TiF_4 (284°C). Once the reactor had cooled to approximately 25°C, the inlet and outlet valves were closed and the reactor was left to cool to room temperature. The reacted sample was then transferred to a crucible and heated in a crucible furnace to 600°C for 3 hours with a 6.4°C/min. The reacted sample was then characterized by XRD, SEM, EDS, and wet chemical analysis for microstructure, morphology and chemical composition respectively.

Chemical analysis of Al, Ca, Fe, K , Mg, Na and Pb were performed by DC ARC method. Si, Ti, and Sr were measured by ICP methods which were performed on a Baird ICPOES instrument and were dissolved using a lithium tetraborate fusion. F was measured by pyrohydrolysis followed by ion Chromatography. Ba was calculated after an impurity scan was completed by a DC ARC method and was calculated by difference.

About 0.075g reacted frustules (converted to TiO_2) were then mixed with $Ba(OH)_2 \bullet 8H_2O$ with varying Ba/Ti ratios. The mixture was placed in a glass vial and placed in a 100 mL glass bottle (Pyrex* Brand Reusable Laboratory Bottle) with a high temperature lid and sealed in an argon atmosphere to prevent CO_2 contamination. The sealed bottle was then placed in a crucible furnace where it was heated to 120°C at 0.32°C/min, and a 10 hour soak time. Once the furnace cooled to room temperature, the converted barium titanate ($BaTiO_3$) frustules and excess $Ba(OH)_2 \bullet 8H_2O$ were placed in a 50 mL plastic centrifuge tube and filled with dionized water. Excess $Ba(OH)_2$ was dissolved in dionized water for about two hours. The frustules were allowed to settle for over an hour. The supernatant was removed with a 50 mL pipette and the process was repeated 4 more times. In the last washing cycle, the suspension was vacuum-filtered through a Whatman qualitative filter paper. Reacted frustules were collected and dried at 98°C. Dried samples were characterized for phase, morphology, and composition.

The same procedure was followed for the conversion of titania (TiO_2) frustules to $SrTiO_3$ with a few minor variations. For the $SrTiO_3$ conversion, in addition to $Sr(OH)_2 \bullet 8H_2O$ and titania frustules, 4mL of water were added per gram of $Sr(OH)_2 \bullet 8H_2O$. The reaction temperature was also increased from 120 to 160°C. The rest of the procedure remained changed.

2.3 Results and Discussion

2.3.1 SiO_2

The as received silica frustules were pyrolyzed in order to remove the organic matter. Figure 3 (a) demonstrates how the as received frustules have a thin coating of organic waste attached to them as well as demonstrates the excess amount of small broken pieces. In Figure 3(b) there is significantly less organic material and broken frustule debris. This is a

result of heating the frustules to 600°C and continues settling cycles. It is noted that this process does not remove all broken pieces but does remove a significant fraction of them.

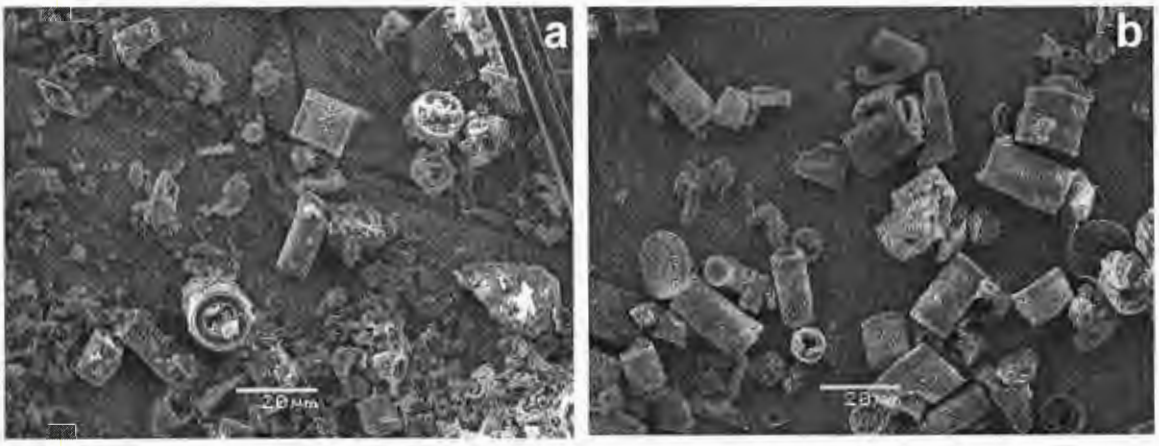

Figure 3. SEM micrograph a) as received natural silica frustules. As can bee seen from the micrograph there is a large number of broken frustules and organic materials. b) Pyrolyzed silica frustules. As can be seen from the micrograph there is a great reduction in organic material and broken frustules.

The chemical composition of the pyrolyzed frustules was determined by chemical analysis (NSL Analytical Services, Inc., Cleveland, Ohio). The results showed that the frustules were made primarily of SiO_2 (92% by wt.) and the remaining composition of other oxides in the following amounts: 3.34% Al_2O_3, 1.16% Fe_2O_3, 1.11% CaO, 0.7% Na_2O, 0.52% MgO and 0.46% K_2O. An XRD diffraction pattern of the pyrolyzed frustules show that they are indeed amorphous from the broad absorption seen in Figure 4. There is a small peak around 28 degrees shown in the figure which is believed to be from a small amount of albite ($NaAlSi_3O_8$).

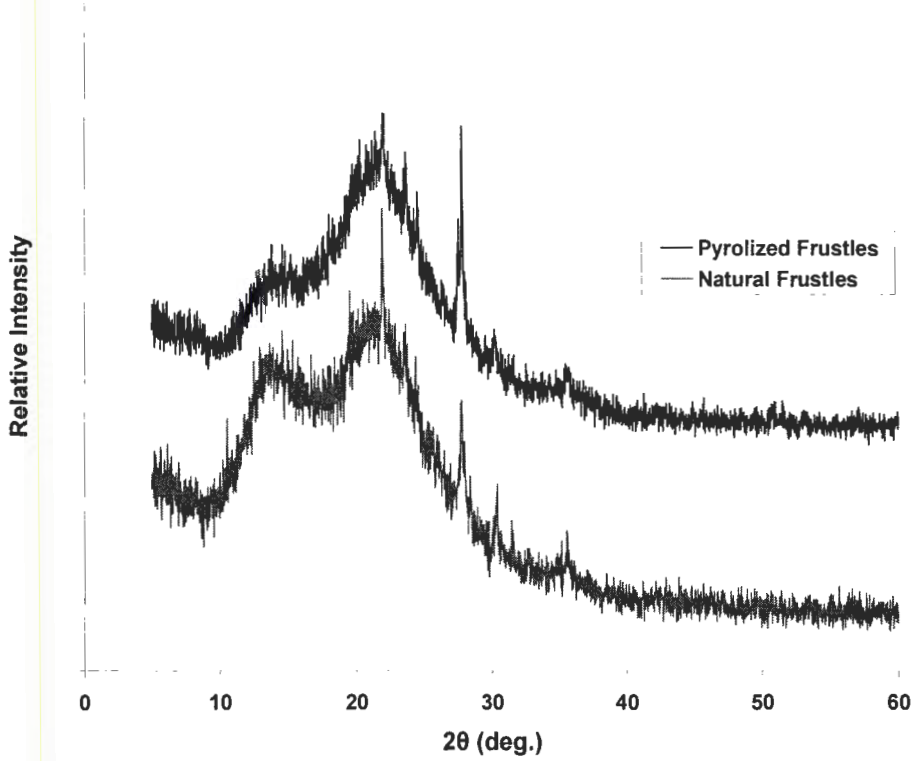

Figure 4. XRD scan of amorphous pyrolyzed silica frustules. The small peak at around 28 degrees is from crystallized albite $NaAlSi_3O_8$.

Although frustules surface areas have been reported up to 258 m^2/g [18] the pyrolyzed silica frustules used in these reactions had surface areas of 25 m^2/g which were measured from multipoint nitrogen gas adsorption and using the BET method.

2.3.2 $TiOF_2$

Figure 5 displays the XRD pattern of the frustules after reacting with TiF_4. The pattern shows that the reaction forms an intermediate compound $TiOF_2$ according to the presumed chemical reaction:

$$TiF_4(g) + \tfrac{1}{2} SiO_2(s) \rightarrow TiOF_2(s) + \tfrac{1}{2} SiF_4(g) \quad \Delta G°(327°C) = -221.524 \text{ KJ/mol}$$

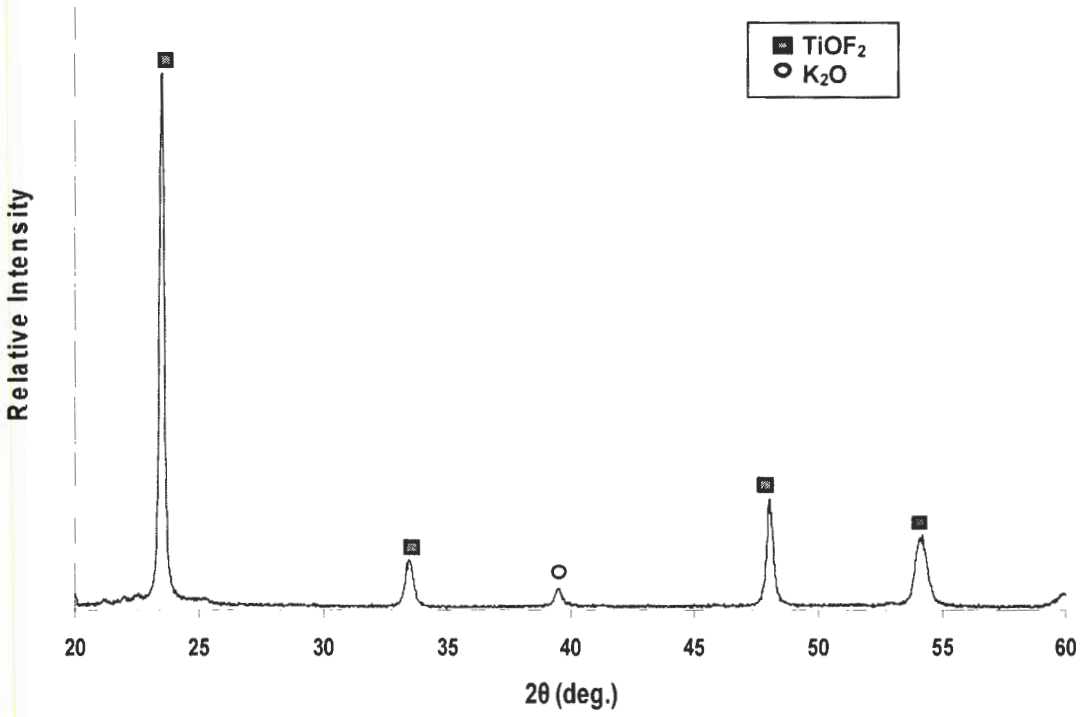

Figure 5. X-ray diffraction pattern of frustules after exposure to TiF_4 gas at 330°C.

The broad peak (2Θ ~20) observed in original frustules is largely absent. Since the reaction temperature is much lower than the pyrolysis temperature and much lower than the crystallization temperatures we have seen before, absence of SiO_2 can only be attributed to reaction with TiF_4 and removal as gaseous byproduct, possibly as SiF_4 as indicated in the above chemical reaction. This resulted in the formation of $TiOF_2$ and a small amount K_2O seen at approximately 39 deg. that is naturally occurring in the silica frustules. From the chemical equation it can be seen that for every SiO_2 the reaction produces two $TiOF_2$. Using this equation the predicted molar volume ratio of $2\bullet TiOF_2:SiO_2$ is 2.4. This is a very significant expansion from SiO_2 to $TiOF_2$ however, as demonstrated from Figure 6, frustules still retain the shape and fine features of the original SiO_2 frustules.

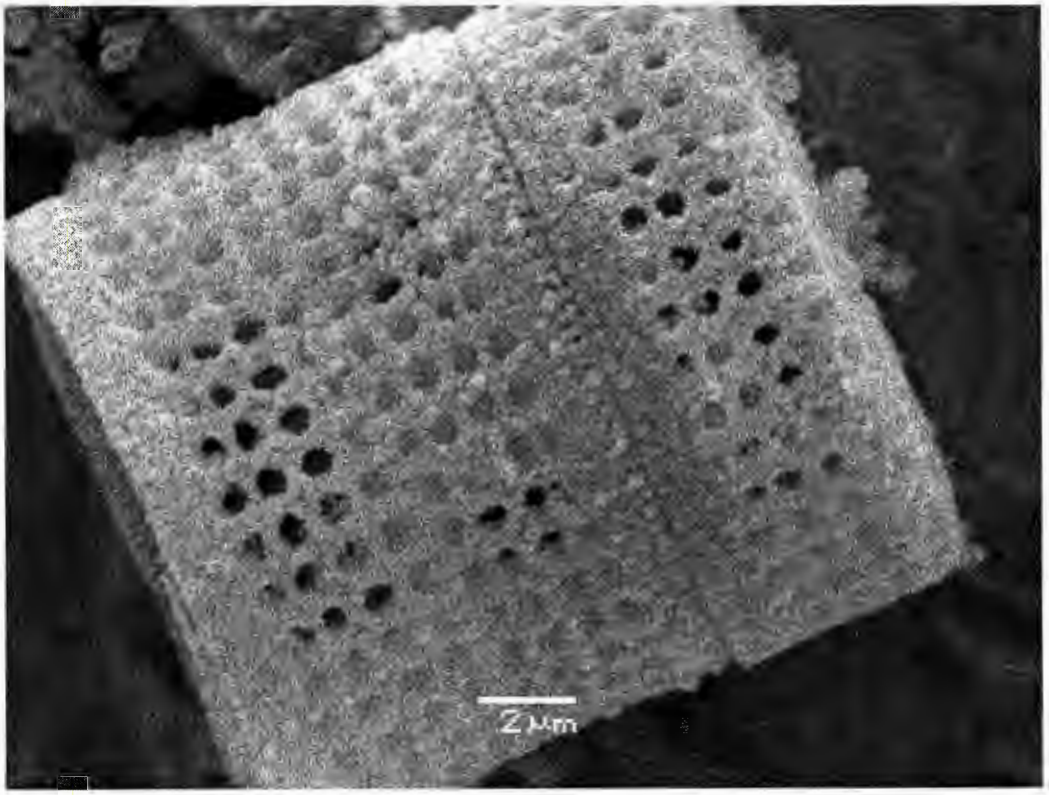

Figure 6. SEM secondary image of frustules after exposure to TiF_4

Energy dispersive spectroscopy (EDS: Oxford Instruments, INCA mics/x-stream/SEM TVA3, Concord, Massachusetts) was used to assess the chemical composition of the reacted frustules. As seen in Figure 7, Ti, O, Au, and F constitutes the majority of the frustule composition. The Au signal is from the gold coating on the sample. In addition, there are minor peaks due to Zn and Cu which are from the bronze sample holder. The elements Al and K are natural impurities found in the frustules, and the Si is a small amount of unreacted Si impurity.

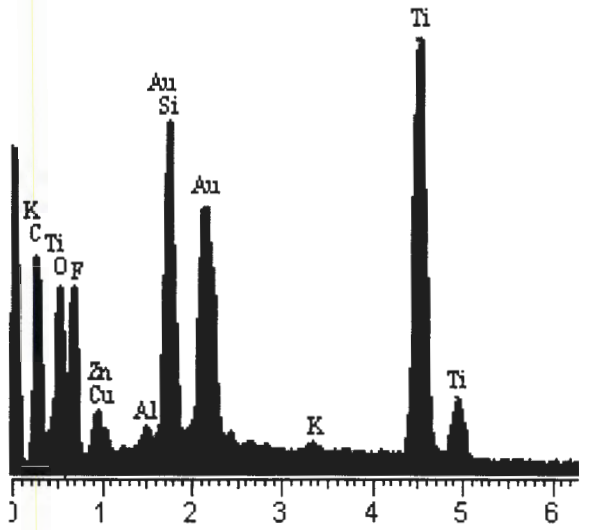

Figure 7 Energy Dispersive Spectrum of frustules after TiF_4 reaction. Note major peaks are associated with Ti, O, and F. The peak marked as Au is due to gold coating, and Zn and Cu peaks are from the sample holder Au

2.3.3 TiO_2

Once the intermediate product was identified as $TiOF_2$, the sample was heat treated at 600°C in air to convert titanium oxyfluoride to titania (TiO_2). TiO_2F frustules reacted with water in the atmosphere under the following presumed reaction:

$$TiOF_2 + H_2O(g) \rightarrow TiO_2(s) + 2HF(g) \qquad \Delta G°(600°C) = -257.2 \text{ KJ/mol}$$

This completed the conversion of silica frustules to titania. X-ray diffraction pattern (Figure 8) shows that the primary phase was indeed anatase (TiO_2) the low temperature form of titania. Although one would assume oxygen displaces fluorine in the lattice, oxidation of fluoride with molecular oxygen is thermodynamically not favored. Instead, it is believed that a small amount of water vapor in the air is responsible for conversion of oxyfluoride to titania as illustrated in the above chemical equation.

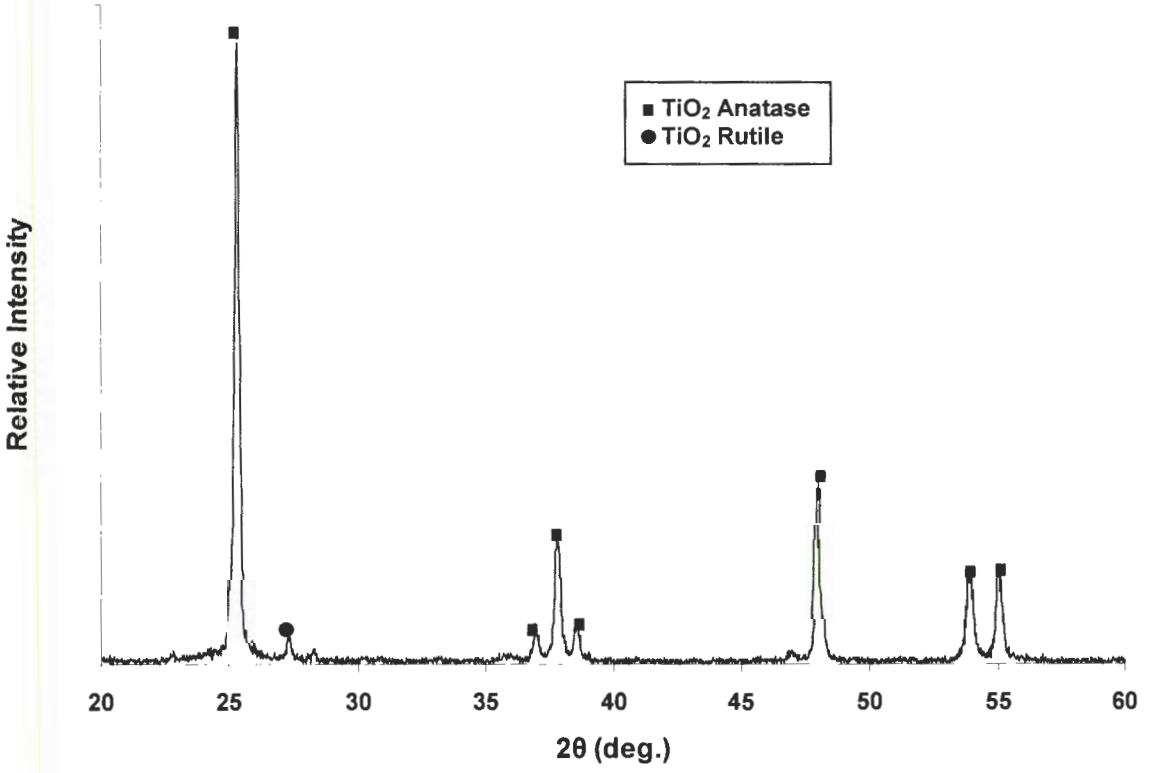

Figure 8. X-Ray Diffraction pattern of frustules after 600°C heat treatment in air for 3 hours. All the major peaks can be assigned to anatase as marked. The remaining peak at around 2Θ = 27° is due to rutile.

Figure 8 was also used to calculate the average crystallite size of the frustule grains by employing the Scherrer formula: $D=0.9\lambda/(\beta\cos\theta)$, were D is the calculated crystallite size and λ is the X-Ray wavelength for K_α radiation and β is the true peak broadening measured at the full-width at half maximum. Using the formula the average crystallite size was found to be 39.5±11.4 nm

Shape retention of the original frustule was verified by SEM as shown in Figure 9. Clearly, not only the overall shape is retained but also a number of the smaller (down to nanoscale) features, including ridges, and pores. However, the structure does look slightly more granular then the original silica frustule. This might be attributable to nanocrystalline TiO_2 compared to amorphous hydrated SiO_2 grains. It should also be noted that smaller broken piece over the large frustule (presumably from another frustule) also shows nanometer remnant of original diatom features. EDS spectrum of the converted frustule is

given in Figure 10. The main elements detected are Ti, O, and Au. Once again, the Au is from the gold coating on the sample. The Zn, Cu, and C peaks are due to the sample holder used, and the Al and K peaks are from natural impurities found in the original silica frustules.

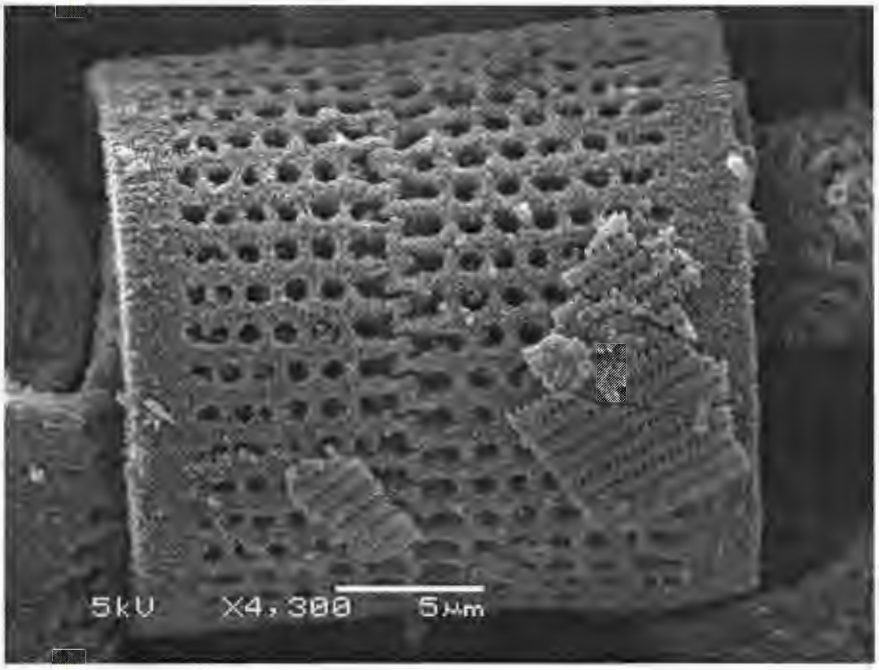

Figure 9 SEM micrograph of titania anatase frustules after 600°C heat

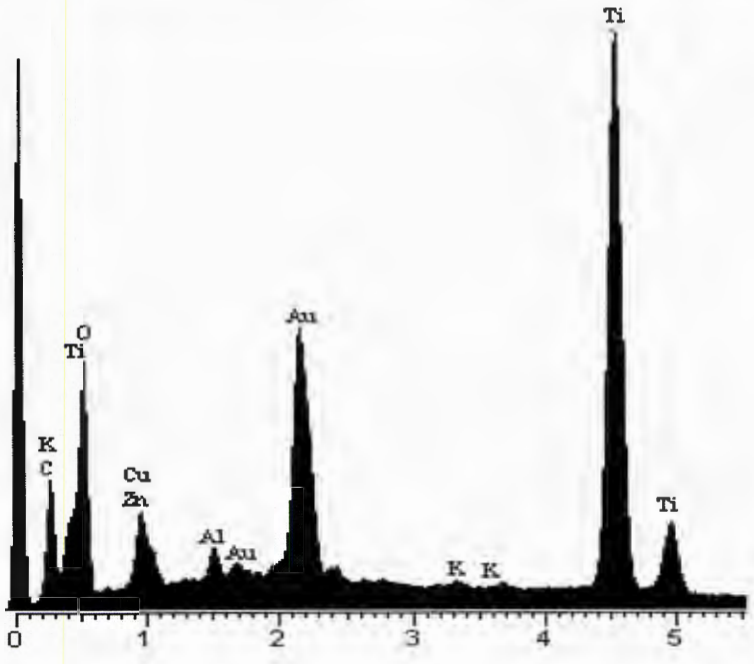

Figure 10 Energy Dispersive Spectrum of frustules after 600°C reheat in air.

A chemical analysis of the converted TiO_2 frustules was performed and the results are shown in Table 1. Explanation of the methods used is described in the $BaTiO_3$ and $SrTiO_3$ sections. From Table 1 it can be seen that the main elements are Ti and O which are the desired elements and the remainder impurities found naturally in the titania frustules with a small amount of F that was not fully removed from the burn out process.

Table 1 Results of chemical analysis of TiO_2, $BaTiO_3$, and $SrTiO_3$ frustules after conversion, reported in at%.

	Ba	Sr	K	Si	Mg	Na	Ca	Fe	F	Al	Ti	O	Other *
TiO_2	0.00	0.01	0.04	0.05	0.16	0.47	0.53	0.67	1.21	2.6	28.1	66.2	0.11
$BaTiO_3$	19.12	0.22	0.02	3.38	0.13	0.10	0.21	0.23	0.07	0.3	16.2	59.9	0.26
$SrTiO_3$	0.00	18.22	0.04	0.83	0.29	0.10	0.26	0.43	0.14	1.0	18.7	60.0	0.31

Other is reported in wt%, it was not possible to convert to at% because of unknown molecular weight.*

2.3.4 $BaTiO_3$

Anatase frustules were converted $BaTiO_3$ or $SrTiO_3$ by a hydrothermal reaction using barium hydroxide or strontium hydroxide, respectively. Excess water was not added to the $BaTiO_3$ conversion, for experiments showed the percent of conversion decreases as excess water was added. In this reaction a 3:1 ratio of $Ba(OH)_2$ to TiO_2 was used. This ratio was determined through experimentation and XRD data which together found that lower Ba:Ti ratios resulted in more retained TiO_2 a plausible chemical reaction for conversion of TiO_2 to $BaTiO_3$ is given by:

$$Ba(OH)_2 \bullet 8H_2O(l) + TiO_2(s) \rightarrow BaTiO_3(s) + 9H_2O(l) \quad \Delta G°(120°C) = -61.2 \text{ KJ/mol}$$

In order to calculate the theoretical molar volume change the above equation has to be taken into consideration. According to the above equation for ever mole of SiO_2 two moles of $TiOF_2$ is produced which is later changed into TiO_2. Therefore for every mole of SiO_2 is produces two moles of $BaTiO_3$. The molar volume ratios of $2*BaTiO_3$:SiO_2 is 2.8.

Although this is a large expansion the system supports such a large expansion and maintains its overall shape and internal fine details as seen in Figure 11. One might claim

that the pores in the $BaTiO_3$ frustule is smaller than that in TiO_2 and SiO_2 frustules, perhaps due to large volume change during TiO_2 to $BaTiO_3$ conversion.

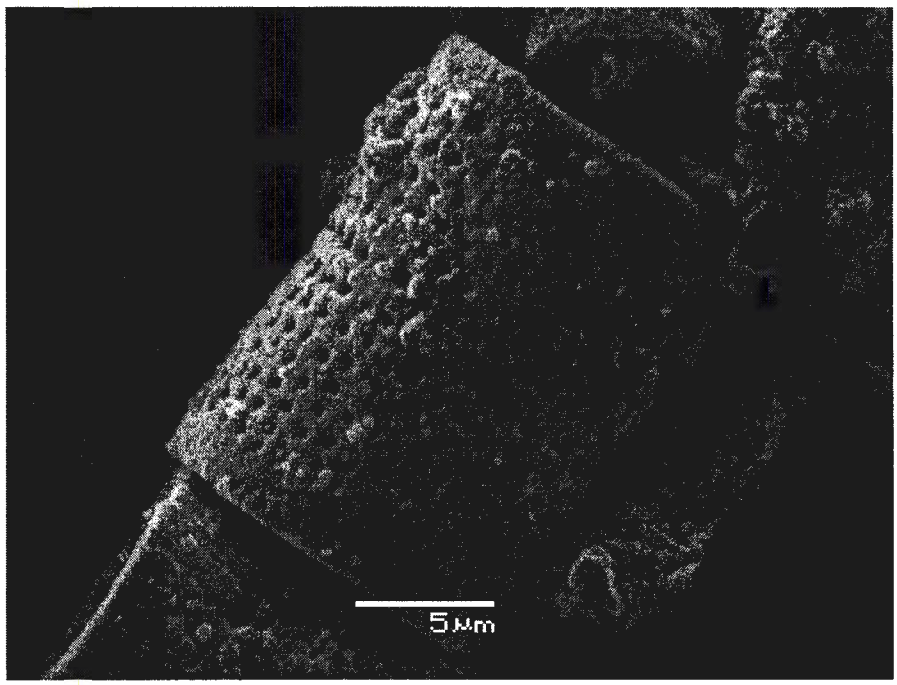

Figure 11. SEM secondary image of converted $BaTiO_3$ frustule

The EDS spectrum of a typical $BaTiO_3$ frustules indicate that the major peaks are due to Ba, Ti, and O (see Figure12). Unfortunately, the Ba and Ti peaks almost coincide making even a semiquantitative estimate of Ba/Ti ratio impractical. The carbon peak at low energies is either due to carbon coating of the frustules for imaging or from CO_2 contamination leading to $BaCO_3$ formation [11]. In some cases small Si peaks were also observed due to incomplete conversion of SiO_2 to $TiOF_2$ during exposure to TiF_4 .

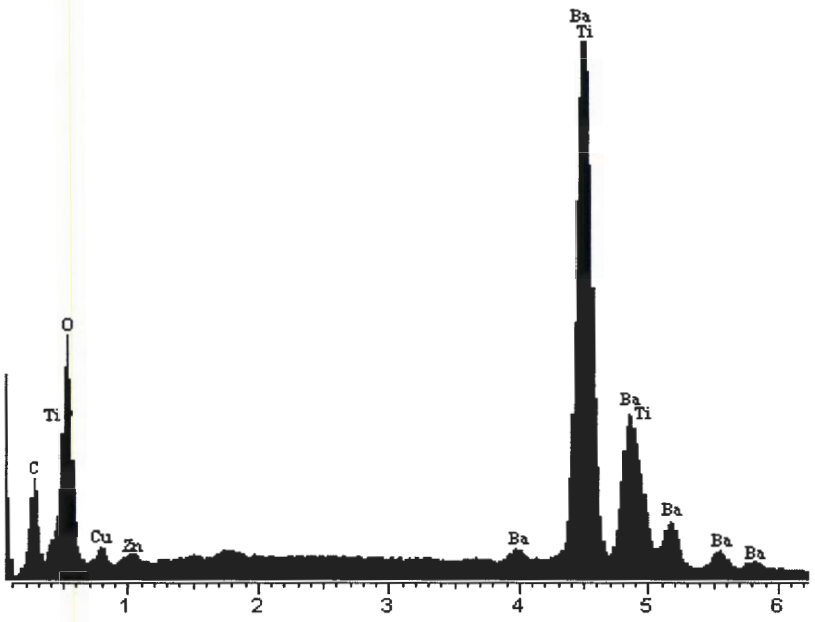

Figure 12. A typical EDS spectrum of $BaTiO_3$ frustule. Note major constituents of reacted frustule are Ba, Ti, and O along with carbon (coating or atmospheric contamination or both) and small amounts of Cu and Zn from sample holder.

Transmission electron microscopic (TEM) examination of reacted frustules revealed the internal structure of the frustules and size of the $BaTiO_3$ crystallites. Figure 13 along with several other images of the same sample were analyzed and the average grain size was measured to be 76nm±14. As discussed before, the crystalline size calculated from X-ray diffraction line broadening was 29nm±3.9. The discrepancy between the two numbers may be a result of the difficulty of TEM calibration and/or bias in the TEM micrograph towards larger grains than small individual crystallites measured in XRD. Selected area electron diffraction image of the same sample is shown in Figure 14. The diffraction pattern matches that of $BaTiO_3$ planes. The resolution of the diffraction image is not sufficient to discriminate whether $BaTiO_3$ is tetragonal or cubic phase. The weak ring pattern may be a function of the high defect structure or the nanocrystalline structure of the $BaTiO_3$ as a result of mild processing conditions employed.

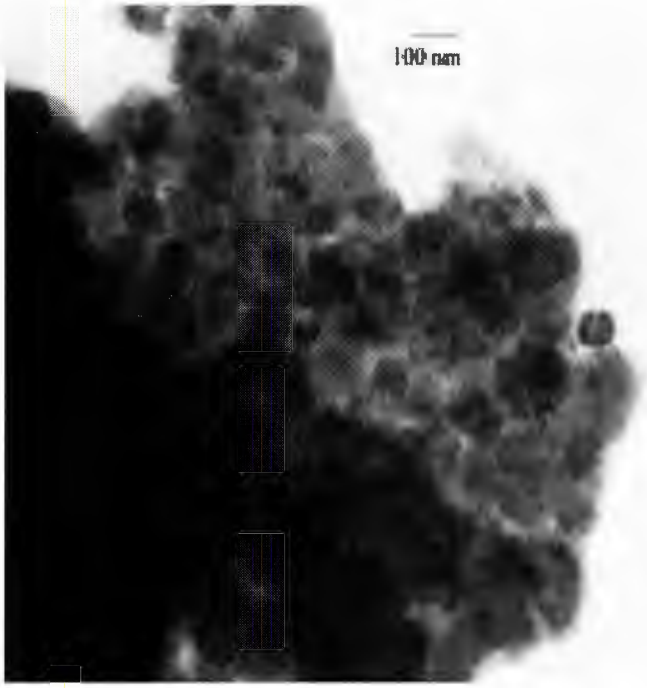

Figure 13. TEM image of $BaTiO_3$ sample. Nanocrystalline nature of the microstructure is clearly illustrated.

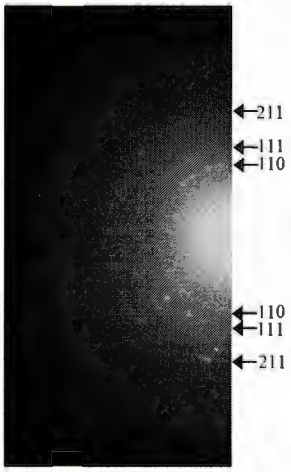

Figure 14. Selected area electron image of $BaTiO_3$ frustule

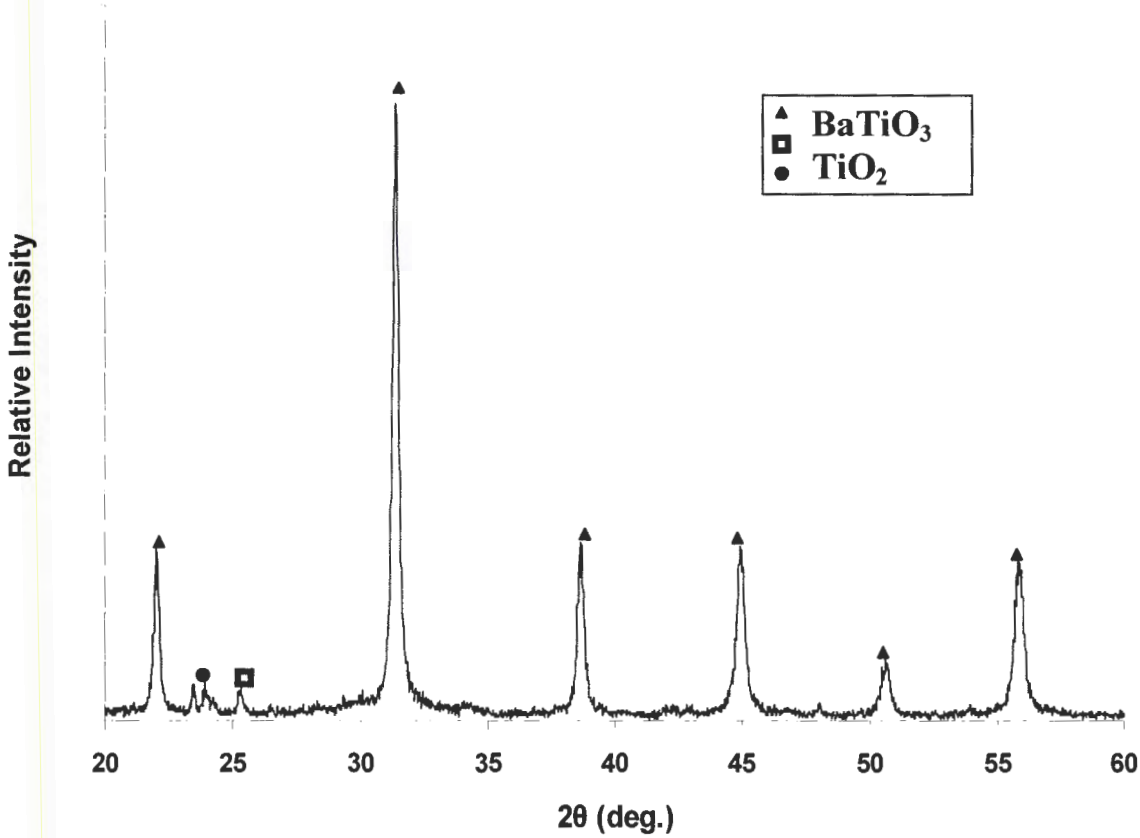

Figure 15. X-ray diffraction pattern of $BaTiO_3$ frustules. The primary phase is $BaTiO_3$ with trace amounts of anatase (TiO_2) and $BaCO_3$ are also observed.

An X-ray diffraction pattern of the $BaTiO_3$ frustules is presented in Figure 15. Three phases were observed: $BaTiO_3$, TiO_2, and $BaCO_3$. $BaTiO_3$ is the major component and is the desired phase. The $BaTiO_3$ pattern belongs to the cubic phase instead of the tetragonal phase which is the thermodynamically stable phase at room temperature. The formation of cubic $BaTiO_3$ from a hydrothermal process is not uncommon [10,14,19]. This phenomenon was originally attributed to the retained OH^- on oxygen sites combined with existence of cation vacancies. High temperature annealing at 900°C for 15 hours removed the hydroxide ions, but the material remained cubic. This opened doubt into the hypothesis of retained OH^- since it was not understood why the charge compensating cation vacancies were retained even after the hydroxyl ions were removed [19]. Only annealing at temperatures higher than 1000°C resulted in transformation to the tetragonal phase upon cooling to room temperature [20]. In

these experiments, crystallite growth was not taken into consideration. However, others reported that cubic phase is stabilized at room temperature if the crystallite size is below 190nm [19, 21]. Since the crystallite size obtained in this study is significantly below this critical size (see Figure 13) it is not unusual to retain the cubic phase. The mechanism for cubic phase stabilization of nanocrystalline $BaTiO_3$ has not been established yet but it is claimed that excess surface energy contributions to the relative free energies of the tetragonal and cubic structures play a dominant role as the crystallite size gets smaller. According to this claim, the grain growth induced by high temperature annealing allows cubic-to-tetragonal phase transformation upon cooling to room temperature [19].

A small amount of anatase (TiO_2) remains unreacted after the conversion reaction. Apparently, the reaction was not driven to completion and still possessed some retained titania after 10 hours of reaction time. Although a great deal of care has been exercised in processing, the small amount of $BaCO_3$ is believed to have formed from atmospheric CO_2 contamination. Reduction of $BaCO_3$ contamination in hydrothermally synthesized $BaTiO_3$ has been achieved by calcinations at higher temperatures [22, 23] or by leaching with formic acid [10].

Table 1 summarizes the results of chemical analysis conducted on $BaTiO_3$ frustules. As expected the three major constituents are Ba, Ti, and O. The ratio of O:Ba:Ti is close to 3:1:0.8 close to the stoichiometric O:Ba:Ti ratio but slightly deficient in Ti. If one assumes that Si is occupying the Ti sites and adds Si to the Ti content, the ratio becomes 3:1:1. Alternatively, the excess Ba (relative to Ti) may be attributed to excess $Ba(OH)_2$ that was not removed during the washing process or to $BaCO_3$ which was detected in the XRD pattern. The XRD pattern also showed some retained anatase so not all of the titanium is in $BaTiO_3$.

The mechanism of $BaTiO_3$ formation by reaction of $Ba(OH)_2$ with TiO_2 is believed to proceed by formation of a surface $BaTiO_3$ layer followed by diffusion of Ba^{2+} through the product $BaTiO_3$ layer [11]. For higher reaction rates larger specific surface areas and smaller grains are most favorable. This is important to take into consideration as specific surface area can vary significantly depending on the species of diatom frustules used. For example, *thalassiosira descipiens* has been reported to have a specific surface area of 258 m^2/g [18] while the frustules used in this work had a specific surface area of 25 m^2/g. The reaction rate

is also dependent on the crystal structure of the reacting TiO_2. Rutile is the thermodynamically more stable phase, and hence, has a lower reactivity with $Ba(OH)_2$ in aqueous solutions then anatase. Therefore, in order to maximize conversion, anatase has to be the majority phase used in conversion [24]. Since the transformation from anatase to rutile is an irreversible reaction and can occur anywhere from 400°C to 1200°C, it is very sensitive to processing-related parameters [25]. Although the second step of the reaction, i.e., conversion of $TiOF_2$ to TiO_2 has been carried out at 600°C, the titania produced was a nanocrystalline anatase phase. Therefore, processing of the titania frustules as low a temperature as possible is desirable for efficient conversion to $BaTiO_3$. Indeed, most methods employed for $BaTiO_3$ synthesis involve much higher reaction temperatures. Hertz reported that at the high $Ba(OH)_2$ concentrations (i.e. $[Ba^{++}] \geq 1M$, which is what was used in this work), the diffusion of Ba^{++} through the product $BaTiO_3$ layer is fast enough to ensure that the TiO_2 interface is saturated with Ba^{2+}. This implies that the topochemical reaction of Ba^{++} with TiO_2 at the interface (with a simultaneous insertion of $O^{=}$ or OH^{-}) as the rate determining step. Extending reaction time to between 24 and 72 hours has been reported to carry the reaction to full completion [11]. It appears that a reaction time of 24 hours would have also led to complete conversion in this study.

2.3.5 $SrTiO_3$

Like the $BaTiO_3$ conversion, the titania frustules were characterized before use in the $SrTiO_3$ reaction. The conversion to $SrTiO_3$ was attempted using a method similar to that used in $BaTiO_3$ formation with the exception that $Sr(OH)_2 \bullet 8H_2O$ rather than $Ba(OH)_2 \bullet 8H_2O$ was used as a reactant. One extra change was the addition of excess water in the $SrTiO_3$ reaction. Unlike its $BaTiO_3$ counterpart, excess water proved to increase the percent conversion in the $SrTiO_3$ reaction. The proposed overall reaction is shown below.

$$Sr(OH)_2 \bullet 8H_2O(l) + TiO_2(s) \rightarrow SrTiO_3(s) + 9H_2O(g) \quad \Delta G°(160°C) = -108.0 \text{ KJ/mol}$$

Like the $BaTiO_3$ conversion, a significant volume change was estimated in going from SiO_2 to $SrTiO_3$. The theoretical molar volume ratio of $2SrTiO_3$:SiO_2 is 2.6. A significant portion of this volume change is associated with the second step of the reaction i.e., from TiO_2 to $SrTiO_3$. The theoretical molar volume ratio of $SrTiO_3$:TiO_2 is 1.9 However, the

volume change was smaller then that of $BaTiO_3$ conversion Thus, less distortion or lower stress levels are expected from conversion of SiO_2 to $SrTiO_3$ than the $BaTiO_3$ conversion.

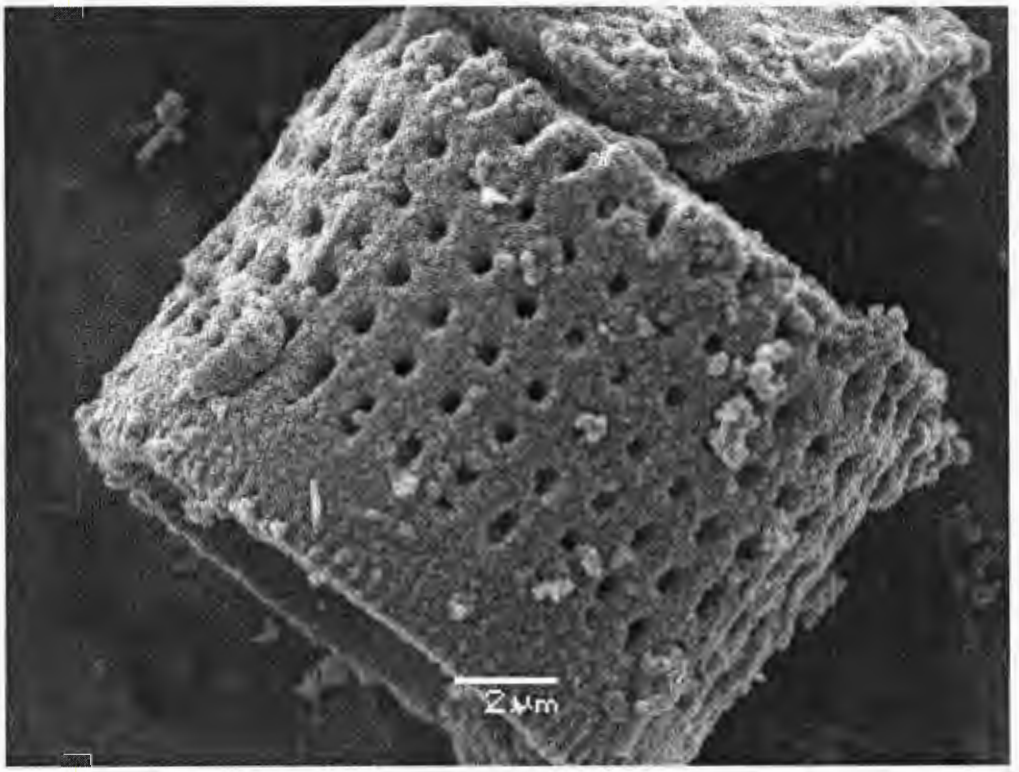

Figure 16. SEM secondary image of converted $SrTiO_3$ frustule

Figure16 shows SEM image of a reacted frustule. As was the case with the $BaTiO_3$ conversion, the micrograph shows that many of the distinct features like ridges, pores and interlacing features of the original frustule are retained through the conversion. Again, as for $BaTiO_3$, the micrograph reveals distinct features of grains compared to the smooth SiO_2 frustule microstructure. This grainy structure is believed to have carried over from the TiO_2 precursor as shown in Figure 6. There are a few small particles on the surface of the frustules, most likely debris from the broken diatoms. The EDS spectrum (Figure 17) shows Sr, Ti, and O as the dominant elements. Other elements are from the substrate (Zn, Cu) and coating (Au) as discussed before. Of the two remaining elements, carbon is either from the coating on the substrate or from $SrCO_3$ formed by possible atmospheric contamination of CO_2 as in the $BaTiO_3$ case. Although the exact source of Fe is unclear, it could be from the 1.16% Fe content of the as-received silica frustule.

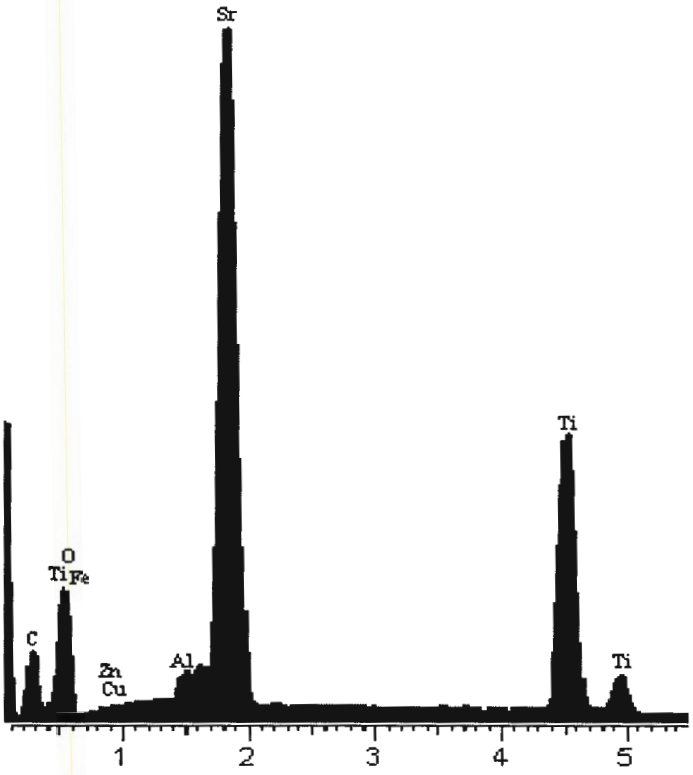

Figure 17. EDS spectrum of $SrTiO_3$ frustule

An x-ray diffraction pattern of $SrTiO_3$ frustule is shown in Figure 18. It is evident that $SrTiO_3$ is the dominant phase and a small amount of unreacted TiO_2 remained.

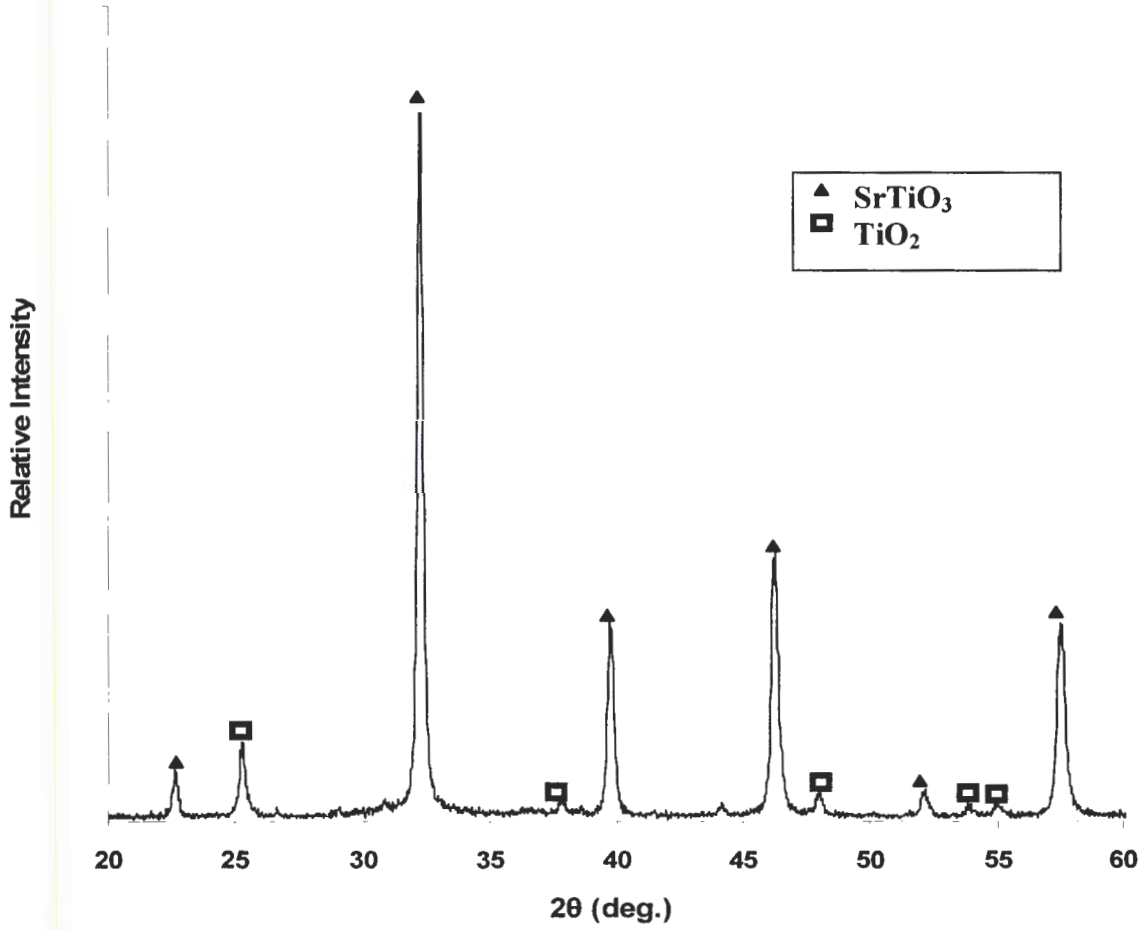

Figure 18. X-ray diffraction pattern of converted $SrTiO_3$ frustules. Note the major phase is cubic $SrTiO_3$ with minor component being unreacted anatase (TiO_2). This XRD pattern is taken from the same sample as seen in Figure 16.

In the $SrTiO_3$ conversion, boiling water was used to decrease the CO_2 concentration to prevent the formation of $SrCO_3$. The same application could be used in $BaTiO_3$ production but was not done in this study. As a result less $SrCO_3$ was formed which can be seen in Figure 18

The chemical analysis of $SrTiO_3$ frustules is given in Table 1. The table shows that the three most prevalent elements are O, Sr, and Ti with a O:Sr:Ti ratio of 3:0.91:0.93. Since there is some retained titania (see Figure 18) and chemical analysis indicate almost identical concentration of Sr and Ti, the Sr content that is not from $SrTiO_3$ may be in the form of $Sr(OH)_2$ or the small amount of $SrCO_3$ that may have formed from retained CO_2 in the boiled

water. Neither of which was detected by XRD. The other elements are naturally occurring in the original frustules. The small amount of silica is from the unreacted silica.

Although the conversion to $SrTiO_3$ from the in-situ hydrothermal reaction has not been studied to the same extent as the conversion to $BaTiO_3$, many of the same observations apply. For example, for higher conversion rates anatase is preferred over the rutile phase [26]. Like $BaTiO_3$, the same overall reaction occurs with the Sr^{2+} ions reacting with the TiO_2 on the surface of the particle which creates a $SrTiO_3$ shell through which the Sr^{2+} ions must diffuse to react with the TiO_2 at the $SrTiO_3$ /TiO_2 interface. However, this reaction is reported to have slow kinetics [14] and therefore may need even longer times than $BaTiO_3$ to react fully. The XRD and chemical analyses data of $SrTiO_3$ and $BaTiO_3$ show that the Ba:Ti ratio is higher then the Sr:Ti ratio which would suggest that longer reaction times should be used in $SrTiO_3$ conversions verses $BaTiO_3$ conversions. But, because we can not assume that all the Ba, Sr and Ti is in a 1:1 ratio no, solid conclusions about kinetic differences between $SrTiO_3$ formation versus $BaTiO_3$ formation can be made. Like the $BaTiO_3$ conversion, it was observed that the converted $SrTiO_3$ was also in the cubic phase at room temperature. However, unlike $BaTiO_3$, the cubic-to-tetragonal phase transformation temperature for $SrTiO_3$ is below room temperature (T_c= 105K), and it is not clear at this stage if the synthesized $SrTiO_3$ will show transformation when cooled below the transformation temperature.

2.4 Conclusions

Conversion of silica frustules to TiO_2, $BaTiO_3$, and $SrTiO_3$ using a gas-solid displacement reaction was studied. Conversion of pyrolyzed frustules to TiO_2 was realized in two stages: in the first step frustules reacted with TiF_4 to form $TiOF_2$ which then converted to TiO_2 (anatase) by a heat treatment in air. Morphology and microstructural details of the original diatoms have been retained through these processes. The titania frustules were then converted to $BaTiO_3$ hydrothermally with $Ba(OH)_2 \bullet 8H_2O$ at 120°C for 10 hours. Conversion to $BaTiO_3$ was nearly complete and it is believed that higher temperature and/or longer reaction times will lead to complete conversion. $BaTiO_3$ formed in this process showed cubic crystal structure which is attributed to nanoscale crystallite size (~70nm) [19]. Extensive

coarsening of the $BaTiO_3$ frustules to a particle size of 190 nm or greater would possibly result in tetragonal $BaTiO_3$ at room temperature. This may lead to loss of frustule shape.

Conversion to $SrTiO_3$ was performed with the same procedure as the one employed for $BaTiO_3$ except excess water was added to the mixture before mixing and the mixture was heated to 160°C instead of 120°C. Like $BaTiO_3$, nearly complete conversion of SiO_2 frustules to cubic $SrTiO_3$ with the original frustule shape was achieved. Since the normal tetragonal to cubic transition is below room temperature, observation of the cubic phase is not surprising.

The present work demonstrated that with further experimental refinement, solid-gas displacement reactions may be a viable method of micro-scaled piezoelectric synthesis.

References

1. Roach, J., *Nanotech Gadgets to be built by Algae?* National Geographic News, 2005.
2. Rotter, G.L.C., Chih-hug, Jeffryes, Clayton; Liu,shu-hong; Gutu, Timothy; Jiao, Jun. *Cellular biosynthesis of nanostructed semiconductor materials*. in *229th ACS National Meeting*. 2005. San Diego, CA: American Chemical Society.
3. Hildebrand, M., *Biological processing of nanostructured silica in diatoms.* Progress in Organic Coatings, 2003. **47**: p. 256-266.
4. Hildebrand, M., *Prospects of Manipulating Diatom Silica Nanostructure.* Journal of Nanoscience and Nanotehcnology, 2005. **5**: p. 146-157.
5. Armbrust, E.V.B., John A.; Bowler, Chris; Green, Beverley R.; Martinez, Diego; Putnam, Nicholas H.; Zhou, Shiguo; Allen, Andrew E.; Apt, Kirk E.; Bechner, Michael; Brzezinski, Mark A.; Chaal, Balbir K.; Chiovitti, Anthony; Davis, Aubrey K.; Demarest, Mark S.; Detter, J. Chris; Glavina, Tijana; Goodstein, David; Hadi, Masood Z.; Hellsten, Uffe; Hildebrand, Mark; Jenkins, Bethany D.; Jurka, Jerzy; Kapitonov, Vladimir V.; Kroeger, Nils; Lau, Winnie W. Y.; Lane, Todd W.; Larimer, Frank W.; Lippmeier, J. Casey; Lucas, Susan; Medina, Monica; Montsant, Anton; Obornik, Miroslav; Parker, Micaela Schnitzler; Palenik, Brian; Pazour, Gregory J.; Richardson, Paul M.; Rynearson, Tatiana A.; Saito, Mak A.; Schwartz, David C.; Thamatrakoln, Kimberlee; Valentin, Klaus; Vardi, Assaf; Wilkerson, Frances P.; Rokhsar, Daniel S., *The genome of the diatom Thalassiosira pseudonana: Ecology, evolution, and metabolism.* Science, 2004. **306**(5693): p. 79-86.
6. Patel, K.S., H.T.S., *Ceramic Semiconductors for Gas Detection.* Key Engineering Materials, 1996. **115**: p. 181-190.
7. Nishizawa H., M.K., *Preparation of BaTiO3 thin films using glycolate Precursor.* Journal of Solid State Chemistry, 1997(131): p. 43-48.
8. M. Z. -C. Hu, G.A.M., E.A. Payzant, C.J. Rawn, *Homogeneous (co)precipitation of inorganic salts for synthesis of monodispersed barium titanate particles.* Journal of Materials Science, 2000. **35**: p. 2927-2936.

9. Franco J., G.S., *Ferroelectric crystals*. 1993, New York: Dover Publications, Inc. 402.
10. Kun-Yuan Chen, a.Y.-W.C., *Preparation of barium titanate ultrafine particles from rutile titania by a hydrothermal conversion.* Powder Technology, 2004. **141**: p. 69-74.
11. Hertl, W., *Kinetics of Barium Titanate Synthesis.* Journal of American Ceramic Society, 1988. **71**(10): p. 879-83.
12. Kyohiko Matsushita, A.K., Kiyoshi Sakaue, Isao Takahashi, Hikaru Terauchi and Syuichi Doi, *Effects of BaTiO3 overlayers deposited on SrTiO3 on its 105K phase transition.* Surface and Interface Analysis, 2005. **37**: p. 145-148.
13. Mao, Y., S.B., Sranislaus S. Wong, *Hydrothermal synthesis of perovskite nanotubes.* Chemical Communication, 2003: p. 408-409.
14. Vivekanandan, T.R.N.K. R., *Precipiatiaon of Rutile and Anatase (TiO_2) Fine Powders and Their Conversion to MTiO3 (M= Ba, Sr, Ca) by the Hydrothermal Method.* Materials Chemistry and Physics, 1988. **19**: p. 533-546.
15. Shandhage K. H, M.B.D., Philip M. Huseman, Michael A. Caranna, Heremy D. Clifton, Tracia A. Bull, Timothy J. Heibel, Warren R. Overton, and Monica E. A. Schoenwaelder, *Novel, Bioclastic Route to Self-Assembled, #D, Chemically Tailored Meso/Nanostructures: Shape-Preserving Reactive Conversion of Biosilica(Diatom) Microshells.* Advanced Materials, 2002. **14**(6): p. 429-433.
16. Unocie R. R., F.M.Z., Peter M. Sarosi, Ye Cai and Kenneth H. Shandhage, *Anatase asseblies from algae: coupling biological self-assembly of 3-D nanoparticles structures with synthetic reaction chemistry.* Chemistry Communication, 2004: p. 796-797.
17. Kalem T., M.A., *Bio-Templated Nano-structured Materials*, in *Materials Science & Engineering*. 2004, Iowa State University: Ames. p. 44.
18. Kamantani A., J.P.R., Marine biology, 1979. **55**: p. 29-35.
19. Begg B.D., E.R.V., and Janusz Nowotny, *Effect of Particle Size on the Room-Temperature Crystal Structure of Barium Titanate.* Journal of the American Ceramic Society, 1994. **77**(12): p. 3186-3192.
20. Vivekanandan R., T.R.N.K., *Characterization of Barium Titanate fine Powders formed from hydrothermal crystallization.* Powder Technology, 1989. **57**(3): p. 181-192.
21. Padture N. P., X.W., *Hydrothermal Synthesis of Thin Films of Barium Titanate Ceramic Nano-Tubes at 200C.* Journal of American Ceramic Society, 2003. **86**(12): p. 2215-17.
22. Brzozowski E., a.M.S.C., *Lowering the synthesis themperature of high-purity BaTiO3 powders by modifications in the processing conditions.* Thermochimica Acta, 2002. **398**: p. 123-129.
23. Bera J., D.S., *Formation of BaTiO3 from Barium Oxalate and TiO2.* Journal of Electroceramics, 2003. **11**: p. 131-137.
24. Faff P., G., *BaTiO3 Preparation by Reaction of TiO_2 with Ba(OH)2.* Journal of the European Ceramic Society, 1991. **8**: p. 35-39.
25. Masaru Yoshinaka, K.H., and Osamu Yamaguchi, *Formation and Sintering of TiO2(Anatase) Solid Solution in the system TiO2-SiO2.* Journal of the American Ceramic Society, 1997. **80**(10): p. 2749-53.

26. Changlong Chen, X.J., Dairong Chen, Yuting Zhao, *Effects of precursors on hydrothermally synthesized SrTiO3 Powders.* Materials Research Bulletin, 2001. **36**: p. 2119-2126.

3 Conversion of Silica Frustules to Nb_2O_5

Shannon Dudley and Mufit Akinc
Department of Materials Science & Engineering
Iowa State University, Ames, Iowa 50011

Abstract

Conversion of diatom frustules to Nb_2O_5 by solid-gas displacement reaction was studied. Silica based frustules were exposed to NbF_5 vapors at 330°C which formed niobium oxy-fluoride (NbO_2F) intermediate. Conversion of the intermediate to Nb_2O_5 was attempted in oxygen atmosphere at elevated temperatures led to formation of secondary intermediate Nb_3O_7F along with various off-stoichiometric niobium oxides. Further high temperature heat treatment in oxygen atmosphere yielded Nb_2O_5 and its sub-oxide derivatives accompanied by evolution of $NbOF_3$ which compromised the shape of the original frustules.

3.1 Introduction

Conversion of silica frustules to other oxides which include TiO_2, $BaTiO_3$, and $SrTiO_3$ has been reported in a previous paper [1]. The present work builds on the earlier one that explores a new approach to manufacturing nanostructured microcomponents by using bio-templates. Diatoms, single-celled microalgea, are employed as bio-templates in this research. They consist primarily of amorphous silica with small amounts of Al_2O_3, CaO, Fe_2O_3, K_2O, MgO, and Na_2O. Each diatom species has their own unique complex shape and morphology. Over 100,000 different species of diatom have been claimed to exist [2]. Nature has the ability to assemble nanosize amorphous silica particles into elaborate three dimensional microstructures. Research in genetic engineering may lead to control of the diatom morphology [3] which could revolutionize the micro-manufacturing of nanostructured devices. Use of diatoms as functional nanostructured device or component is limited by the physical properties of silica which makes up more than 90% of the frustule composition. In order to overcome this limitation, shape preserving displacement reaction was used to replace the silicon in the frustules with other elements. Primary purpose of the current research is to

replace silicon with niobium thereby changing the frustule composition from silica-based to niobia-based while preserving the complex shape of the diatom frustule.

Niobium oxide has a large range of applications but two of the most common are as catalysts and sensors. Niobium oxides are known to enhance catalytic activity and also prolong the life of catalysts. Niobium oxide (Nb_2O_5) is used as a catalyst for the oxidative dehydrogenation of propane to propylene [4]. Niobium oxide can be used as a promoter, supporter or as a solid acid. As a sensor, Nb_2O_5 has been reported as a lean-burn oxygen sensor in the 400-800C temperature range and has been reported to have excellent sensitivity and good reversibility for oxygen [5]. It has also been employed as a dopant for other gas sensors.

Sensors based on TiO_2 have a high resistance to lead when dissolved in gasoline which makes it an excellent choice to be used in Air/Fuel ratio control in automobile engines [6]. TiO_2 is being investigated in a wide range of applications including NO_x, NO_2, CO, and CO_2 detection. Research has shown that TiO_2 sensing capacity increases by doping with elements like Pt, Cu, Cr, and Nb. It has also been claimed that impurity ions with high valency, like Nb^{+5}, reduce the oxygen vacancy concentration and inhibit the transformation of anatase to rutile [7]. Addition of Nb to TiO_2 has also been extensively studied for oxygen sensing. Nb addition creates a higher sensitivity at lower working temperatures in Nb-doped TiO_2 sensors. There have also been studies illustrating the possibility of using Nb-doped TiO_2 sensors for CO or alcohol monitoring. The specific mechanism by which Nb doping alters the sensing characteristics of TiO_2 is not clear. However, it is generally accepted that Nb doping affects TiO_2 performance by modifying the microstructure of the base material, controlling the grain growth, and introducing electronic states at the surface or in the bulk which changes the conductivity and the gas sensing properties. Introducing niobium into titania may increase the concentration of electrons as well as induce the creation of a donor level by the formation of defects which include vacancies or interstitial oxygen. This shifts the Fermi level closer to the conduction band [8], which reduces the electrical resistance of TiO_2 but still maintains its n-type behavior unlike the other dopants such as chromium which changes the conductivity of titania to p-type [9]. Frustule conversion to TiO_2 has already been achieved in our laboratory and recently reported [10].

Niobium oxide structure is extremely complicated and demonstrates extensive polymorphism. Amorphous niobium oxide will start to crystallize in a "low-temperature" structure which is referred to as T-phase around 500°C but will crystallize much faster at higher temperatures (to about 830°C). Above 830°C, it forms a "medium-temperature" form referred to as M. Like the T-phase, this crystallization occurs faster at higher temperatures. Finally, at temperatures above 1000°C it transforms to a "high-temperature phase H. These transformations are sluggish, occur at undefined temperatures, presumably affected by trace impurities and/or grain size, and the transformations are irreversible.

There is a homologous series of structures between Nb_2O_5 and NbO_2 with the general formula $Nb_{3n+1}O_{8n-2}$ (n=5, 6, 7, 8). There are also the oxides that are stoichiometrically related to Nb_2O_5 with the chemical formula $Nb_{12}O_{29}$ and $Nb_{94}O_{232}$ which have been reported to posses paramagnetic properties [11]. The distinction between these compositions as stoiciometric separate phases and defective derivatives of Nb_2O_5 is not obvious.

This paper reports conversion of SiO_2 frustules into Nb_2O_5 using the same shape retaining displacement reaction reported in a previous paper [12] used in converting silica frustules to titania. This technique is based on solid gas displacement reaction to retain the unique and complex shape of the frustules while changing the chemical composition. The ultimate goal would be to control and choose the desired frustule shape by genetic engineering while changing the chemistry of the frustules by shape preserving chemical reactions.

3.2 Materials and Methods

Frustules used in this study were same as was used for TiO_2 conversion. The details of pre-treatment of as received diatoms were given in a previous paper [1]. The conversion of silica frustules to Nb_2O_5 is very similar to the conversion of silica frustules to titania [1]. Like the TiO_2 reaction, when SiO_2 is exposed to NbF_5, it forms an intermediate Niobium oxy fluoride, NbO_2F, according to the following proposed reaction:

$$NbF_5(g) + \tfrac{1}{2} SiO_2(s) \rightarrow NbO_2F(s) + \tfrac{1}{2} SiF_4(g)$$

The reaction is carried out in a stainless steel reactor as shown schematically in Figure 1. About 0.08g of SiO_2 frustules and 0.63g of NbF_5 were placed on separate cavities

of the reactor base. The amount of reactants used in this study represents an NbF_5/SiO_2 molar ratio of 2.518. The reactor was sealed in an argon glove box to prevent oxidation of NbF_5 in air and to prevent other gasses from contaminating the reaction. The sealed reactor was then placed in a crucible furnace and heated to 330°C (well above the boiling of NbF_5, T_b=229°C) in an hour and held for 90 minutes in which argon was flown through the reactor in the last 30 minutes at the reaction temperature. Argon is continued to flow though the reactor until the reactor is cooled to 80°C which is the solidification temperature of NbF_5. The reacted frustules removed from the reactor and placed in a ceramic crucible and heated to 1100°C in flowing oxygen to convert NbO_2F (or other intermediate oxy-fluorides) to niobium oxide. Final product was characterized for composition, structure and morphology.

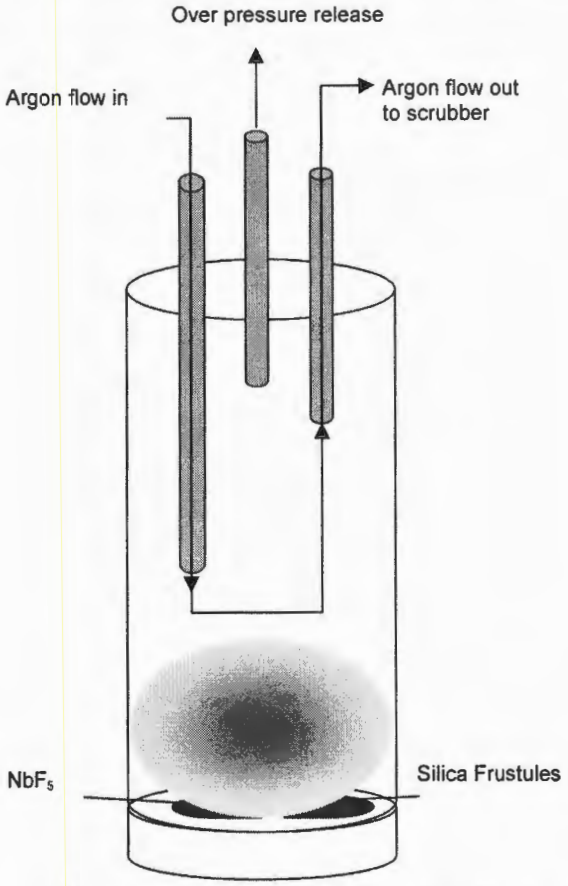

$$NbF_5(g) + \tfrac{1}{2}SiO_2(s) \rightarrow NbO_2F(s) + \tfrac{1}{2}SiF_4(g)$$

Figure 1 Stainless steal reactor used for converting SiO_2 frustules to NbO_2F

3.3 Results and Discussion

3.3.1 Starting Materials

Detailed characterization of the starting materials was discussed elsewhere [1]. Briefly, the diatom frustules consist of hydrated amorphous silica nanograins. After pyrolysis the chemical composition of the frustules showed 92% SiO_2 remaining consisted of other oxides as follows: 3.34% Al_2O_3, 1.16% Fe_2O_3, 1.11% CaO, 0.7% Na_2O, 0.52% MgO and 0.46% K_2O. Even after pyrolysis at 600°C, the starting material was amorphous. Typical frustule morphology used as a starting material is given in Figure 2.

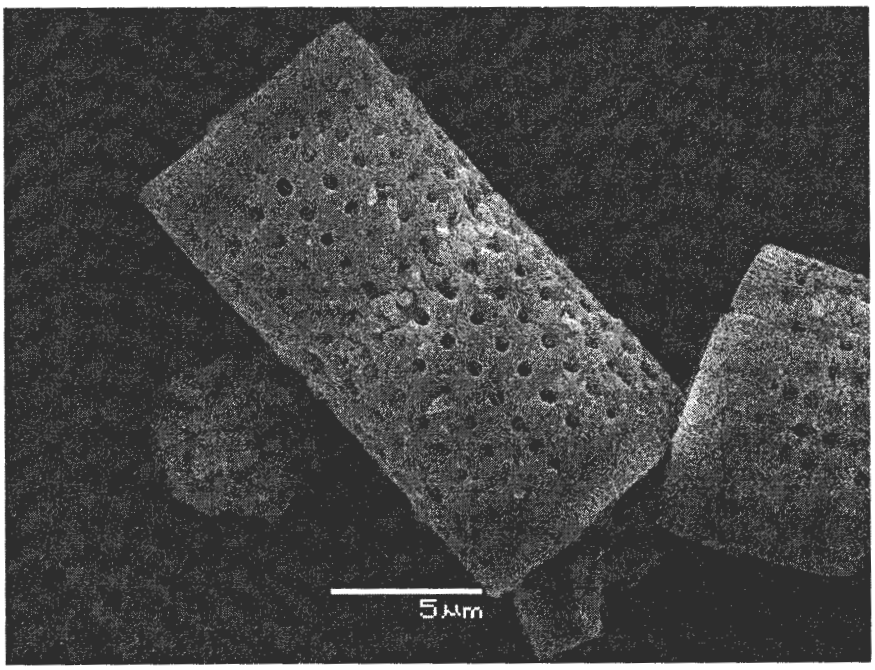

Figure 2. Morphology of starting diatom frustules

3.3.2 NbO_2F

The formation of NbO_2F was observed after exposing the silica frustules to NbF_5(g) at elevated temperatures, presumably undergoing the following reaction:

$$NbF_5(g) + \tfrac{1}{2} SiO_2(s) \rightarrow NbO_2F(s) + \tfrac{1}{2} SiF_4(g)$$

Even though the boiling temperature of NbF_5 is 234°C, there is little reaction between 210-260°C [12] but almost complete reaction was observed at 330°C. Figure 3 shows an

XRD pattern of the reaction product after exposing the silica frustules to NbF_5 at 330°C for 90 minutes. From the figure it can be seen that the amorphous silica is completely converted to a crystalline niobium oxy fluoride as indicated by complete elimination of the amorphous background observed for pyrolyzed silica frustules.

Average crystallite size of the NbO_2F frustule grains was determined by employing the Scherrer formula: $D=0.9\lambda/(\beta\cos\theta)$ on the highest intensity peak in Figure 3, where D is the calculated crystallite size and λ is the X-Ray wavelength and β is the true peak broadening measured at the full-width at half maximum. The average crystallite size was found to be 54±19nm.

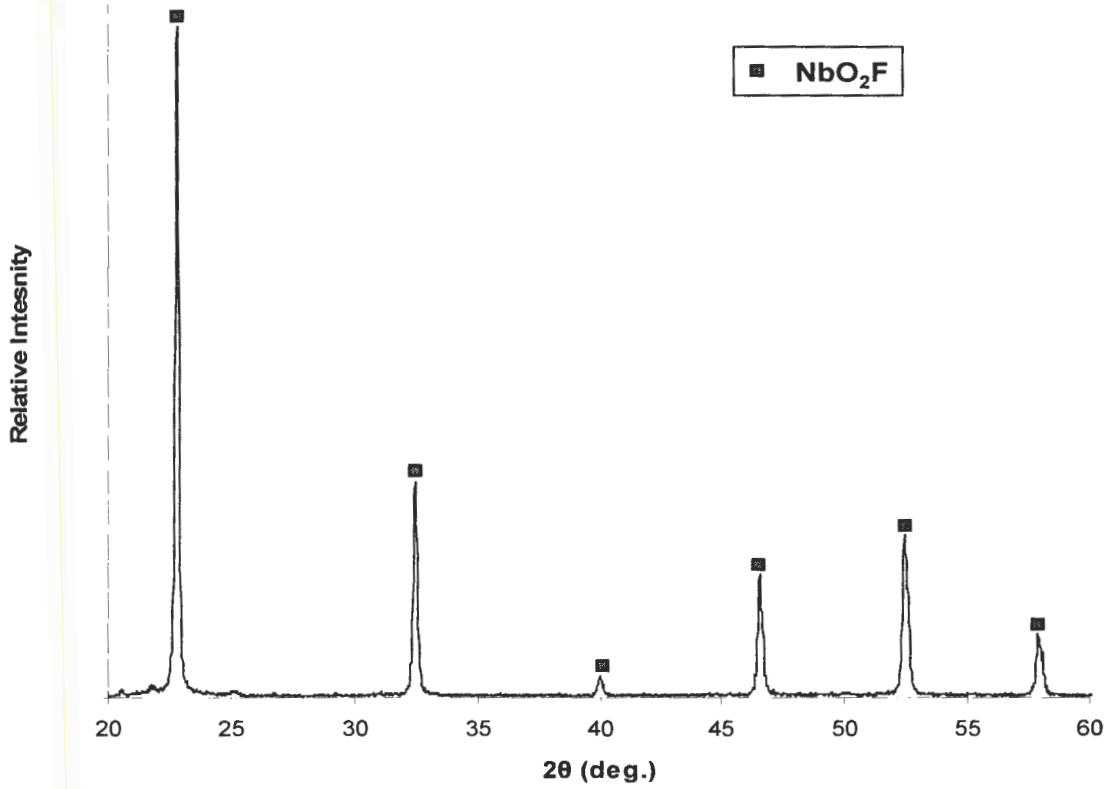

Figure 3. XRD scan of reacted frustules. Amorphous silica is completely converted to crystalline NbO_2F. No other phases were observed indicating a quantitative reaction between SiO_2 and NbF_5 resulting in single phase, crystalline NbO_2F.

As anticipated, the SEM micrograph (Figure 4) shows that the frustules retain their shape after the conversion to NbO_2F. It is clear that not only the overall shape of the frustules

are retained but also the smaller features like the pores and interlocking seam of the two halves are also retained.

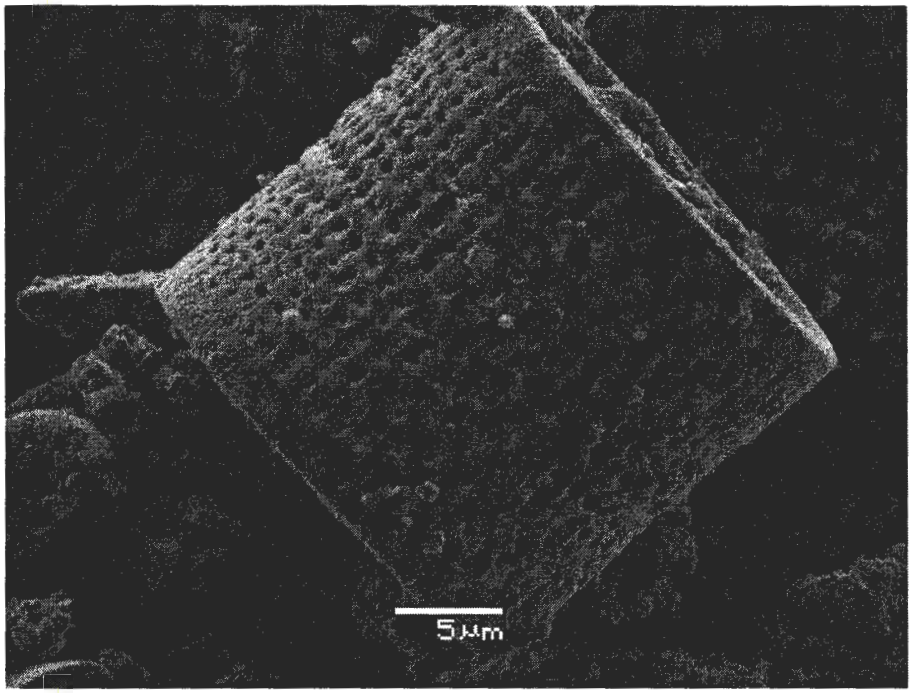

Figure 4. SEM micrograph of NbO_2F frustules after reacting with NbF_5 at 330°C.

Energy Dispersive Spectrum (EDS) of NbO_2F frustules is shown in Figure 5. The spectrum shows only Nb, O, F, and C peaks. The Nb, O and F are from NbO_2F and C is form the carbon coating used during sample preparation. The other elements K, Ca, Fe, and Al are from the original frustule. The peaks for Cu and Zn are from the bronze sample holder. The last element Ti is a trace impurity from the previous TiO_2 runs.

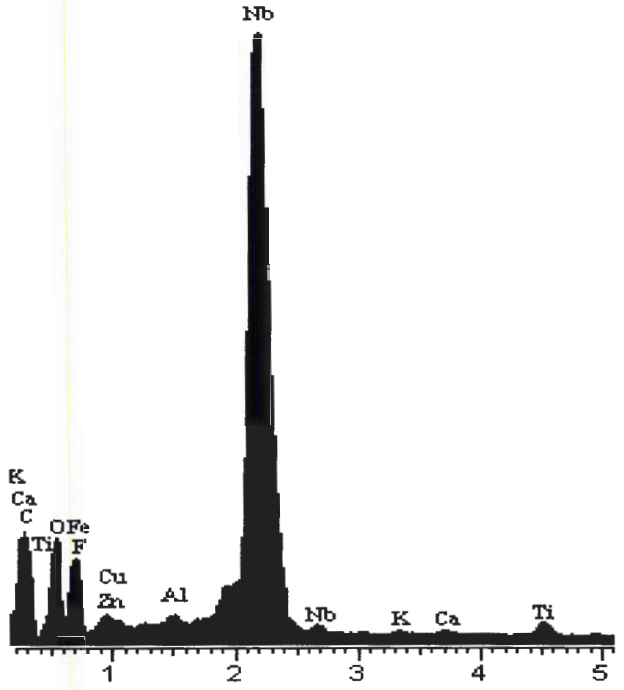

Figure 5. Energy Dispersive Spectrum of NbO_2F frustule. Note the major peaks are of Nb, O, F, and C is from the carbon coating. Other small peaks are naturally occurring elements in the frustules or from the bronze sample holder. The small amount of Ti is due to contamination from previous TiO_2 runs.

NbO_2F (Pm3m, a=0.3902nm) has a ReO_3-type structure which is a defective perovskite-type structure. It is also an n-type semiconductor and has a wide ban gap of E_g~3.1eV and has been reported to be easily doped via H^+ or Na^+ insertion [13].

The conversion of NbO_2F to Nb_2O_5 is a multi-step decomposition. It is claimed to go through the following two step chemical reactions [14].

$$4NbO_2F(s) \rightarrow Nb_3O_7F(s) + NbOF_3(g)$$
$$3Nb_3O_7F(s) \rightarrow 4Nb_2O_5(s) + NbOF_3(g)$$

NbO_2F decomposes to Nb_3O_7F between 750-840°C and then continues to decompose from Nb_3O_7F to Nb_2O_5 between 970-1100°C in dry argon [14].

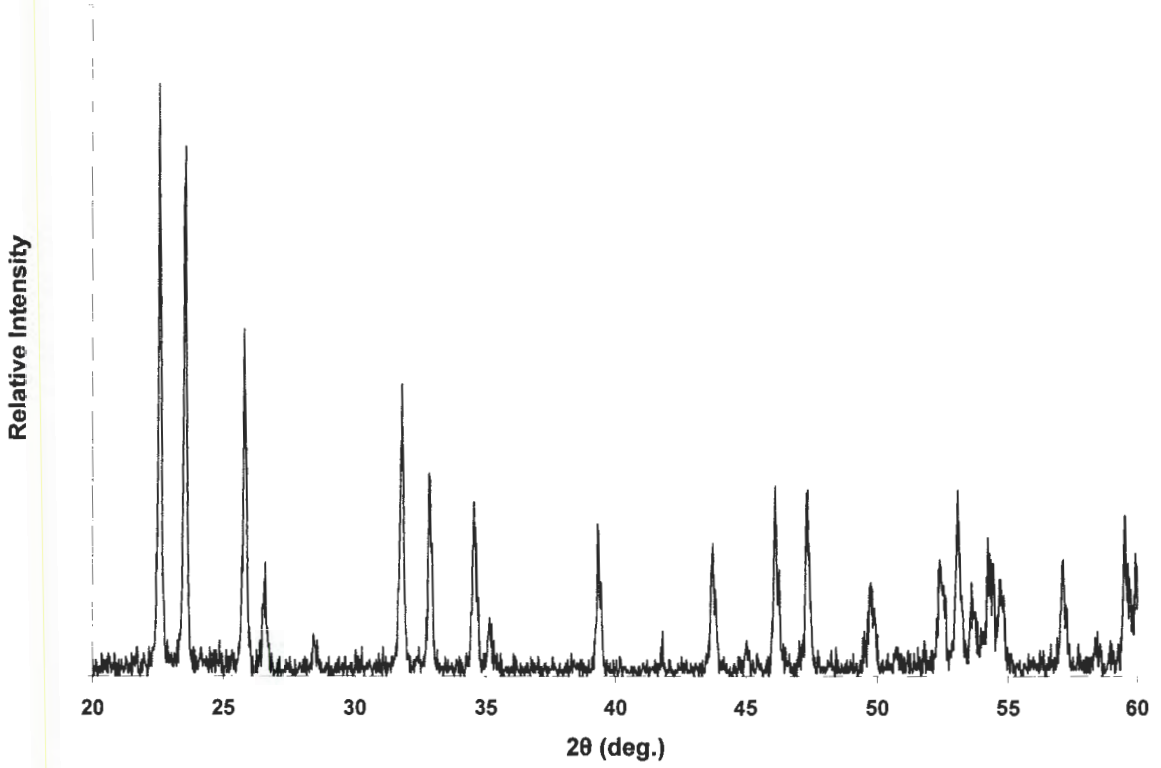

Figure 6. XRD pattern of Nb_3O_7F after oxidation of NbO_2F in air

Figure 6 Shows the XRD pattern of the intermediate NbO_2F after heating to 700°C. The XRD pattern indicates that the NbO_2F oxidation goes through formation of a second intermediate of Nb_3O_7F with a concomitant formation of gaseous $NbOF_3$ in accordance with chemical equation given above. The gaseous $NbOF_3$ is removed from the system by flowing argon over the reaction. Most of our higher temperature heat treatments were carried out in oxygen atmosphere. Figure 7 shows XRD pattern of the frustules heated to 600°C in oxygen. The pattern clearly indicates that the same intermediate Nb_3O_7F phase forms. However, an additional phase appears to form which has been identified as Nb_2O_5 (PDF# 027-1311). This phase has a monoclinic structure and a C2/m space group symmetry [15].

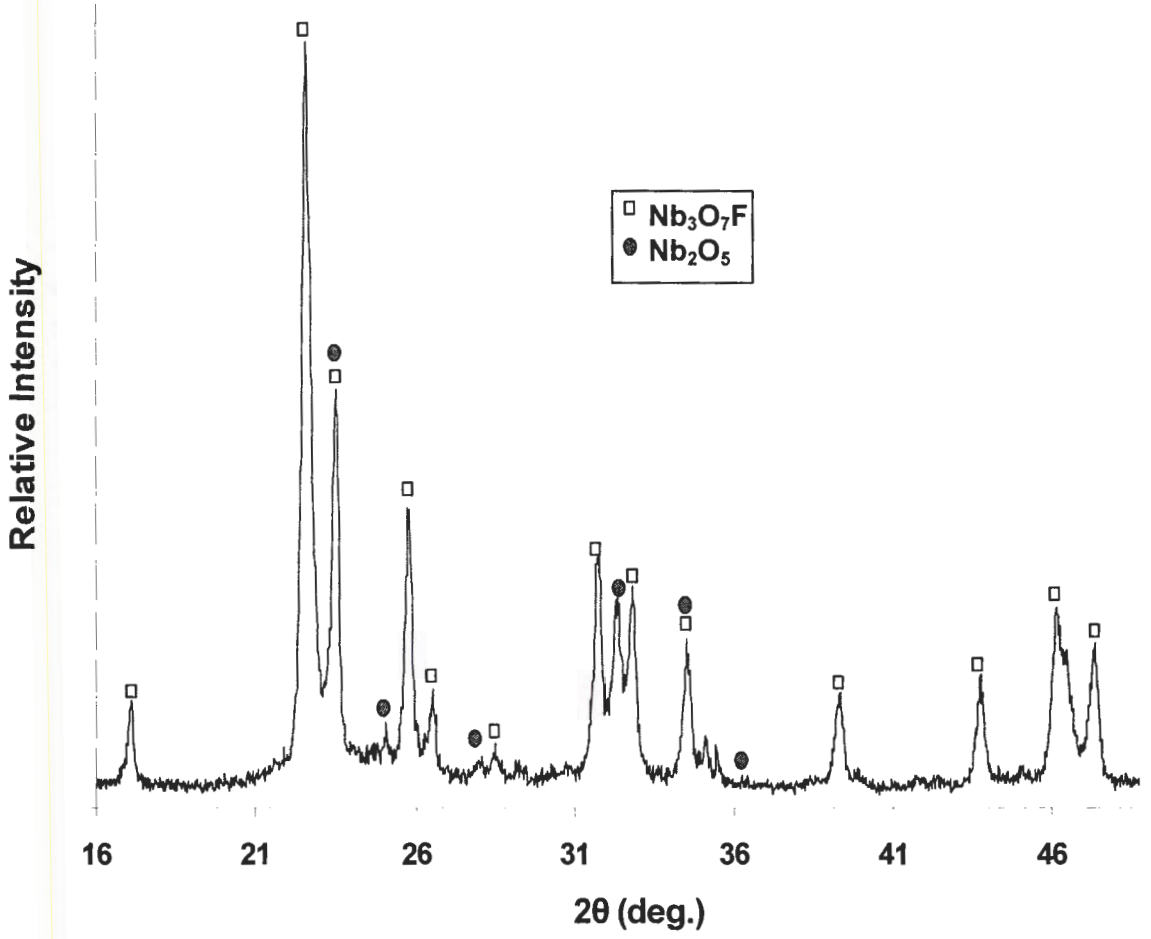

Figure 7. XRD pattern of frustules after heat treatment of NbO_2F at 600C in O_2. The two phases identified are Nb_3O_7F and Nb_2O_5.

3.3.3 Conversion to Nb_2O_5

Further heat treatment at 1100°C in oxygen atmosphere continues to remove the fluorine from the frustule.

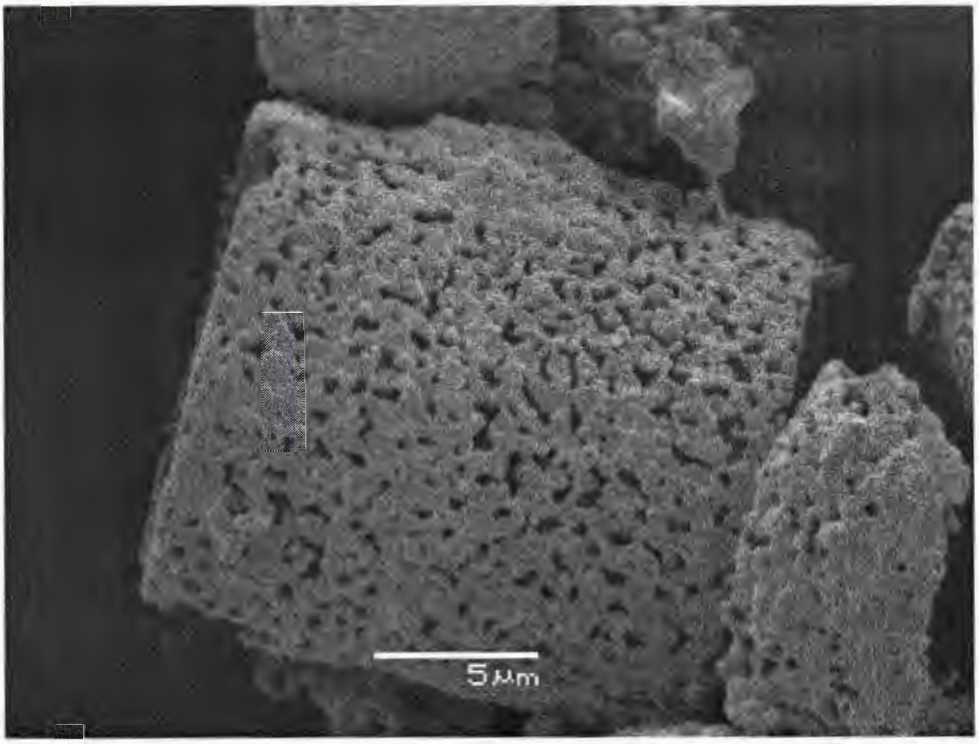

Figure 8. Secondary electron image of frustule after heat treatment at 1100°C for 30 minutes

Figure 8 shows a frustule after being heated to 1100°C for 30 minutes under flowing O_2 atmosphere over the sample. The SEM micrograph clearly shows that although the overall shape of the original frustule was retained, the smaller features like the pores and interlocking seam of the two halves were mostly lost.

Unlike the TiO_2 conversion in which the F is removed without Ti loss, the Nb_2O_5 conversion is associated with significant removal of Nb along with anticipated F removal during heat treatment in oxygen. This is believed to be the reason for the loss of the fine details of the diatom frustule.

Energy dispersive spectrum (EDS) of the frustules indicates that the overall composition of the reacted frustules consists primarily Nb and O as shown in Figure 9.

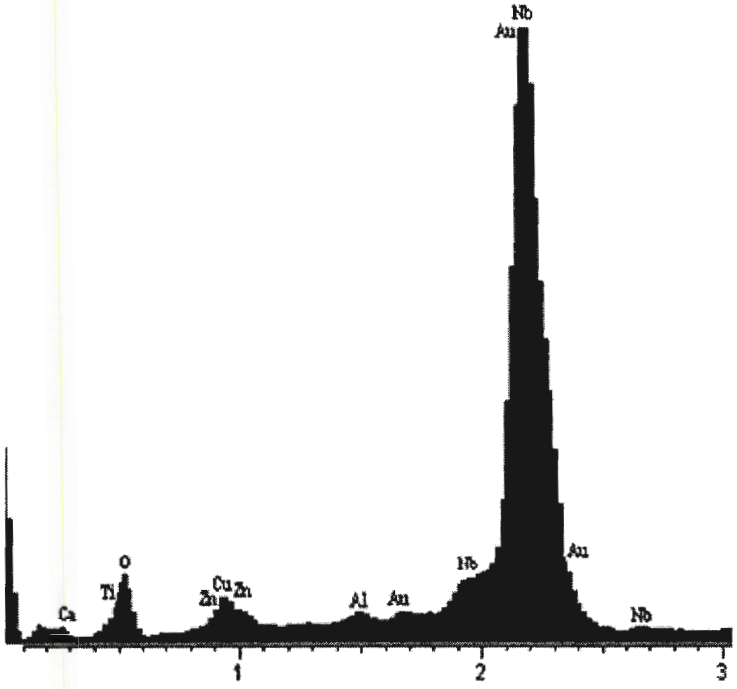

Figure 9. EDS of Nb_2O_5 frustle obtained after heat treatment at 1100°C in flowing oxygen atmosphere.

The other elements shown include Ca, and Al are from the impurities found in the original silica frustules, and Cu and Zn are from the sample holder. Again, the small amount of Ti is believed to be a contamination from the reactor that was previously used in TiO_2 conversions.

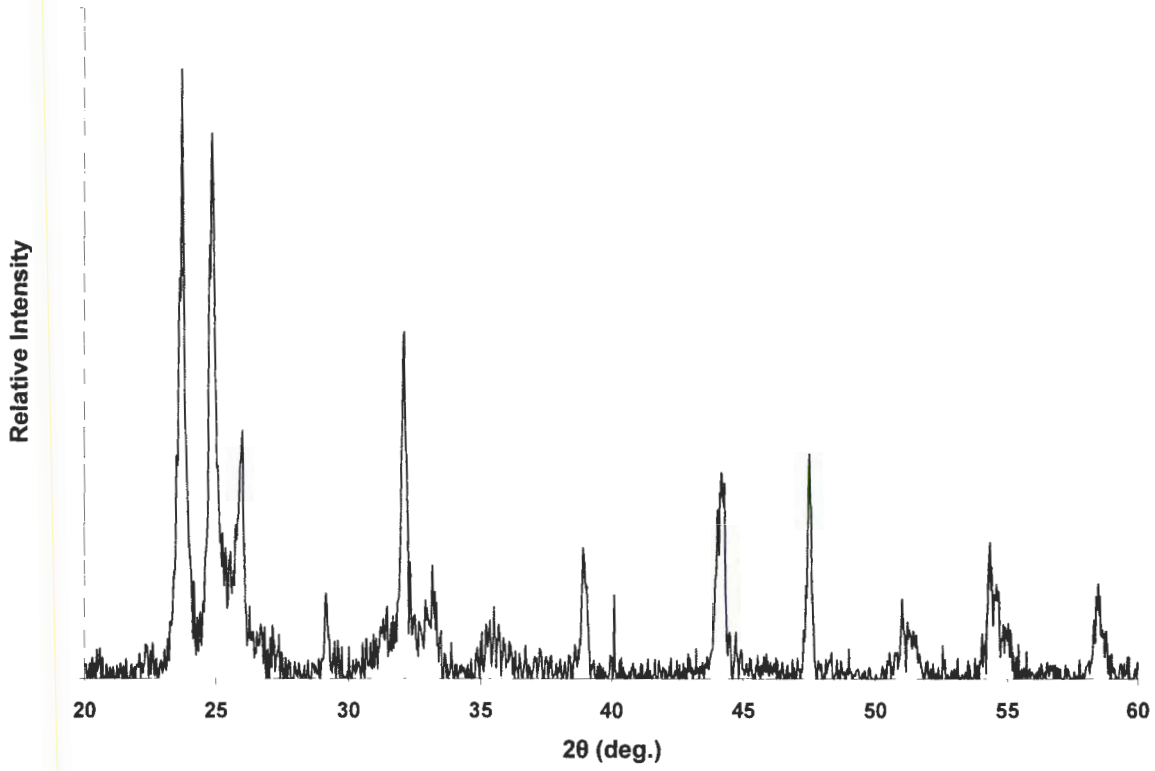

Figure 10. XRD of frustules following NbF_5 reaction and heat treated at1100C in O_2

Figure 10 shows an X-ray diffraction pattern of the final product. It is a mixture of a number of niobium oxide structures which include NbO_2, $NbO_{2.4}$, $Nb_{12}O_{29}$ and Nb_2O_5, and is exceptionally complicated pattern. Niobium has a range of oxidation states from +5 to -1. It is most stable in the +5 oxidation state but +4 oxidation state is found in halide compounds and +2 and +3 is often found cluster compounds based on octahedral M_6X_{12} units [11]. This provides a large variety of niobium oxide compounds some of which are well documented and have crystal structures that are well understood and yet others are not well understood or agreed upon.

Table 2 XRD peak identification of niobium oxide frustule including PDF identification numbers

Phase / PDF# / 2θ	NbO_2 043-1043	$NbO_{2.4}$ 042-0700	$Nb_{12}O_{29}$ 034-1169	$Nb_{12}O_{29}$ 016-0734	$Nb_{12}O_{29}$ 016-0733	Nb_2O_5 032-0711	Nb_2O_5 019-0862
23.723		●	●	●	●	●	●
24.862		●	●	●	●	●	●
25.992	●	●	●	●			
26.698		●		●			
29.155					●		
31.306		●			●		
32.088		●	●	●	●	●	●
33.172		●	●	●	●		
35.35-35.70	●		●	●	●		●
38.907		●	●			●	●
40.1	●	●					
44.18		●	●			●	●
47.511			●			●	●
51.024							●
51.443						●	
54.348							●
54.68						●	
58.491						●	●
64.318						●	●
66.889							●
72.512						●	●
74.152						●	●

NbO_2, $NbO_{2.4}$ and $Nb_{12}O_{29}$ are oxygen deficient compounds compared to Nb_2O_5. For this reason, oxygen was flowed though the furnace instead of argon yet oxygen deficient phases like $NbO_{2.4}$ and $Nb_{12}O_{29}$ were still present in the mixture. Longer times and higher temperatures did not result in single phase stoichiometric Nb_2O_5. Different atmospheres were

also used including dry argon, air, and $H_2O(g)$ rich argon. All results showed a mixture of the same niobium oxide phases. However, there also appears to be multiple crystal structures of individual phases. For example, there are three different polymorphs of $Nb_{12}O_{29}$ that can be matched to the XRD peaks in the figure. Two of these phases are orthorhombic (016-0734, 034-1169) and one is monoclinic (016-0733). There are also two forms of Nb_2O_5 as shown in the above table. With the final two phases identified as NbO_2, $NbO_{2.4}$. Table 1 summarizes the possible phases that can be matched to the diffraction pattern shown in Figure 10. Of all the identified niobium oxide phases, NbO_2 is the most documented structure. In this structure niobium holds a +4 valence state. And is in a tetragonal (I41/a) crystal structure. It also has a distorted rutile structure and is diamagnetic [11]. Unfortunately, all of the peaks that match the niobia frustules also overlap with other identified phases so the presence or the extent of NbO_2 in the system is not known. Unlike NbO_2, the crystal structure of $NbO_{2.4}$ is much less clear. This phase was formed by annealing Nb and Nb_2O_5 for 10-12 days at 1100-1150°C in an evacuated quartz ampoule followed by heating at 1500°C for 3-5 hours [15]. Very little is known about this structure but from the table, it can be seen that many of the peaks found in the niobium oxide frustules match the peak positions given in the reference PDF card. The literature data does not provide any diffraction peaks beyond $2\Theta = 44°$. It is unclear whether this is because there were no peaks beyond $2\Theta = 44°$ or were not reported. The same is true for two of the $Nb_{12}O_{29}$ phases that were matched. No diffraction peak was reported beyond $2\Theta = 36°$. This compound is an oxygen deficient phase which is basically two oxygens are missing for every dozen Nb_2O_5 units ($12Nb_2O_5$-2O). There were three different $Nb_{12}O_{29}$ phases that could be matched to the experimental diffraction pattern. Two of which are orthorhombic and the third is monoclinic. The orthorhombic phase $Nb_{12}O_{29}$ (034-1169) is fairly well understood and has a *Amam* space group. From the table it can be seen that it matches several peaks of the frustules along with the other orthorhombic $Nb_{12}O_{29}$ (016-0734) phase. Both crystal structures share many characteristics including the same unit cell dimensions (a,20.72; b, 28.9; c,3.835). However, $Nb_{12}O_{29}$ (016-0734) posses a different space group symmetry and from the table it can be seen that there are six distinct peak positions that are unique to the individual phases that match the niobia frustle pattern. The last monoclinic $Nb_{12}O_{29}$ (016-0733) phase has a A2/m space group. $Nb_{12}O_{29}$ is an example of

how the niobia system has a variable capacity to form oxygen vacancies. As a result it exhibits a series of crystallographic shear plane structures[16]. The last two phases shown in the table are of Nb_2O_5. One of which has a monoclinic structure (019-0862) however the space group is not reported. Unit cell parameters are reported to be: $a = 21.457$; $b = 7.638$; c = 9.52 and $\alpha = 90$ $\beta = 114.92$. The last phase identified in the table is of Nb_2O_5 (032-0711). Very little information is available for this phase. It even lacks the space group, or unit cell parameters. It is reported to be a medium temperature polymorph of Nb_2O_5.

Although there are many phases in the final product and for many not much known about them, XRD pattern shown in Figure 10 demonstrated that silica frustules can be converted to niobium oxide with various stoichiometries. While the overall morphology and shape of the frustules were maintained, the fine details were lost during reaction presumably due to evolution of various niobium oxy fluorides during heat treatment. Unlike most studies where exceptionally high purity materials can be used and tight tolerances on impurity concentration can be maintained, the frustules employed in this study naturally have approximatel 8% impurities that can greatly affect the crystal structure of the products. Another factor when trying to identify the phases present is the small crystal size of the frustules. The small crystallites result in significant peak broadening which can make peak identification difficult. All these factors contribute to the difficulty of identifying the crystal structures the products formed.

3.4 Summary

Frustule morphology was retained when SiO_2 frustules were converted to NbO_2F by exposing to NbF_5 at 330°C. Heating to 1100°C in O_2 resulted in decomposition of the NbO_2F frustules to Nb_3O_7F. Further heat treatment in oxygen did not yield single phase Nb_2O_5 but rather a mixture of niobium complex oxide phases including NbO_2, $NbO_{2.4}$, $Nb_{12}O_{29}$, and Nb_2O_5 were obtained. Other experiments at different times, temperature and atmospheres produced similar results and none of which produced single phase Nb_2O_5. Numerous niobium oxide phases were reported in recent literature with greatly varied stoichiometry some of which with very little structural information. Yet the XRD patterns exhibit similar patterns and common peaks due to related structures. The two step decomposition of NbO_2F

to Nb_2O_5 with evolution of gaseous $NbOF_3$ presumably leads to loss of fine details of the frustule morphology. Unless the gaseous niobium oxy fluoride evolution is prevented, it is questionable whether the fine details of frustules can be retained for this system.

References

1. Dudley S., *$BaTiO_3$ Conversion*, M.S. Thesis, *Material Science Engineering*. 2005, Iowa State University: Ames.
2. Hildebrand M., *Biological processing of nanostructured silica in diatoms.* Progress in Organic Coatings, 2003. **47**: p. 256-266.
3. Hildebrand M., *Prospects of Manipulating Diatom Silica Nanostructure.* Journal of Nanoscience and Nanotehcnology, 2005. **5**: p. 146-157.
4. Rossa J. R. H., R.H.H.S.a.K.S., *The use of niobia in oxidation catalysis.* Catalysis Today, 1993. **16**(3): p. 503-511.
5. Kohli, A.W., C. C.; Akbar, S. A., *Niobium pentoxide as a lean-range oxygen sensor.* Sensors and Actuators, B: Chemical, 1999. **B56(1-2)**: p. 121-128.
6. Patel K.S., H.T.S., *Ceramic Semiconductors for Gas Detection.* Key Engineering Materials, 1996. **115**: p. 181-190.
7. G.L. Sharma Rajnish K. Sharma, M.C.B., *Effect of Nb metal ion in TiO_2 oxygen gas sensor.* Applied Surface Science, 1995. **92**: p. 647-650.
8. Ruiz A. M., G.D., J. Arbiol, A. Cornet and Joan R. Morante, *Insights into the structural and Chemical Modiffications of Nb Additive on TiO_2 Nanoparticles.* Chem. Mater., 2003. **16**(5): p. 862-871.
9. Ruiz, A., *Study of the influence of Nb content and sintering temperature on TiO_2 sensing films.* Thin Solid Films, 2003. **436**: p. 90-94.
10. Kalem, T., *Bio-Templated Nano-structured Materials*, M.S. Thesis, *Materials Science & Engineering*. 2004, Iowa State University: Ames. p. 44.
11. Ziolek, I.N.M., *Niobium Compounds: Preparation, Characterization, and Application in Heterogeneous Catalysis.* Chemical Review, 1999. **99**: p. 3603-3624.
12. Nieder-Vahrenholz, H.G.S., Harald., *Oxide fluorides of niobium and tantalum.* Zeitschrift fuer Anorganische und Allgemeine Chemie, 1987. **544**: p. 122-6.
13. Hiroshi Mizoguchi, M.O., and Masahiro Hirano, *NbO2F: An oxyfluoride phase with wide band gap and electrochromic properties.* Applied Physics Letters, 2002. **80**(25): p. 4732-4734.
14. Andersson S., A.A., *The Thermal Decomposition of NbO2F.* Acta Chemica Scandinavica, 1965. **19**: p. 2136-2138.
15. *Jade*, Materials Data Inc.: Livermore.
16. Waldron J.E.L., M.A.G., D.A. Neumann, *Structure and electronic properties of monoclinic Ng12O29.* Journal of Physics and Chemistry of Solids, 2004. **65**: p. 79-86.
17. Sandhage K.H., *Anatase assemblies from algae:coupling biological self-assembly of 3-D nanoparticle structures with synthetic reaction chemistry.* Chem. Commun., 2004: p. 796-797.

4 General Conclusions

The overall goal of this research was to replace the silicon in the silica frustules with another appropriate element to form a functional metal oxide. This was accomplished by employing gaseous metal fluorides. Titanium and niobium were used to displace silicon. Reaction of metal fluoride displaced silicon as gaseous silicon tetra fluoride or oxyfluoride while forming metal oxyfluoride solid with similar morphology to that of silica frustules. Conversion of intermediate oxyfluorides to metal oxides was attempted by heat treatment at elevated temperatures in air or other atmospheres. Anatase (TiO_2) obtained in this study was further converted to $BaTiO_3$ and $SrTiO_3$ by reacting with corresponding alkaline earth hydroxides ($Ba(OH)_28H_2O$ or $Sr(OH)_28H_2O$). Relatively high conversion yields were realized for both perovskite syntheses. Conversion of niobium oxyfluoride (NbO_2F) to niobium pentaoxide resulted in loss of fine details of the original frustule morphology.

4.1 $BaTiO_3$ and $SrTiO_3$ Conversion Reactions

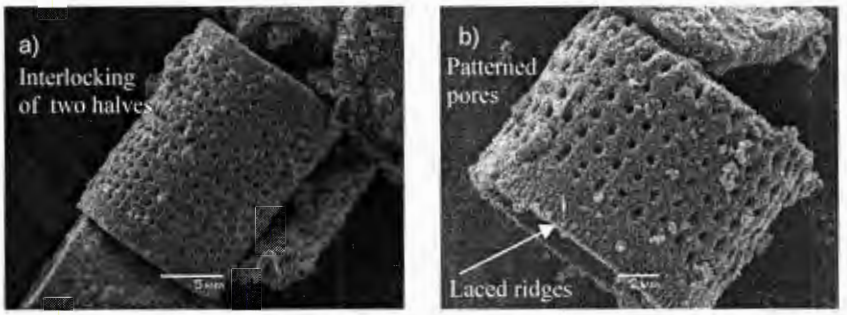

Figure 1 SEM micrographs of a) $BaTiO_3$ frustule and of TiO_2 frustules to $BaTiO_3$ and $SrTiO_3$ was attempted by reacting them with $Ba(OH)_28H_2O$ melt (or $Sr(OH)_28H_2O$ in the case of $SrTiO_3$). In these types of conversion reactions Ba^{2+} or Sr^{2+} along with extra O^{2-} is carried to the titania frustule surface where they react with TiO_2 to form $BaTiO_3$ and $SrTiO_3$. The excess water added significantly increased the conversion to the $SrTiO_3$ but had a reverse effect on $BaTiO_3$ conversion (see Appendix for details). Fraction of TiO_2 converted was estimated from the XRD intensity ratio of Ba(or Sr)TiO_3 -to-TiO_2 peaks. XRD showed that in addition to $BaTiO_3$ and $SrTiO_3$, a small amount of $BaCO_3$ and $SrCO_3$ were also formed presumably from the atmospheric CO_2 contamination. When the reaction was carried out in argon atmosphere all but small amounts of carbonate contamination were eliminated. Reactions resulted

in titanate frustules which retained even the finest details of the original frustules as shown in Figure 1.b) $SrTiO_3$ frustule

Chemical analyses showed that the final products consist mainly of Ba, Ti, and O in the $BaTiO_3$ frustules and Sr, Ti, and O in the $SrTiO_3$ frustules. Slight excess Ba in $BaTiO_3$ frustules may be attributed to either remnant $Ba(OH)_2$ or Ba tied up by residual Si left from the titania conversion. In the $SrTiO_3$ conversion, there was a slight amount of unreacted titania which showed up as small but a distinct peak in XRD pattern.

Overall the conversion of silica frustules to TiO_2 and then to $BaTiO_3$ and $SrTiO_3$ proved successful. The shape of the original frustule was retained with slight grain coarsening. This method of fluoride conversion and later hydroxide conversion proved to be viable methods of conversion and may also be so for future conversions.

4.2 Nb_2O_5 Conversion

The conversion of silica frustules to Nb_2O_5 was very similar to the conversion of silica frustules to titania. Like the titania conversion, silica frustules formed an intermediate oxy fluoride compound, NbO_2F upon exposure to gaseous NbF_5. Unlike titania conversion however, the niobium oxy-fluoride goes through several intermediate reactions during further heat treatment[59]:

$$4NbO_2F(s) = Nb_3O_7F(s) + NbOF_3(g)$$
$$3Nb_3O_7F(s) = 4Nb_2O_5(s) + NbOF_3(g)$$

Evolution of significant quantity of niobium oxy-fluoride products renders shape retention difficult.

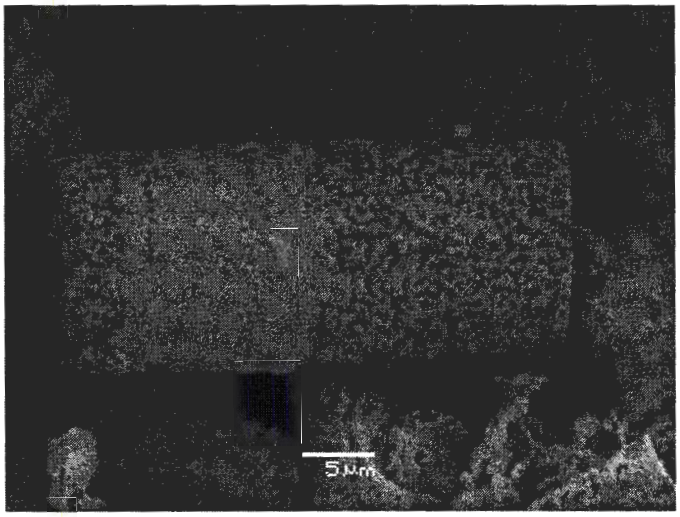

Figure 2. SEM image of Nb_2O_5 frustule

Figure 2 shows the morphology of the Nb_2O_5 frustule. Evolution of gaseous niobium oxy fluorides during the heat treatment cycle is believed to be responsible from the loss of fine details of the frustule morphology.

In summary, this research showed that the transformation of silica frustules to different oxides is possible. This was achieved through gas-solid and liquid-solid reactions. It also proved that the shape retention is also achievable at least for TiO_2, $BaTiO_3$ and $SrTiO_3$, although slight coarsening of the microstructure was observed. Initially there were four main criteria that were taken into consideration for a reaction to be successful: thermodynamically favorable, volume conservation, practical reaction conditions, and ease of separation of desired products. However, the reaction attempted has proved that other requirements are also need to be fulfilled. These include: reaction time and temperature, and the gas atmosphere used in the process. In the case of $BaTiO_3$ and $SrTiO_3$ conversion, it was shown that nearly full conversion may take tens of hours. Ideally, realistic reaction times (reaction times that can be measured in hours not days or weeks) are preferred unless full conversion is not necessary. Also, although separation of byproducts was an important requirement, it was found that the way in which the byproducts are removed is important. The nature of the material was also found to be important. Nb_2O_5 conversion was a good example of this. Existence of multiple valance states for Nb made formation of single phase Nb_2O_5 very difficult. Also, removal of residual fluorine by heat treatment resulted in loss of

shape due to simultaneous loss of Nb and O from the frustule structure. Overall, this research did prove that changing of silica frustules to different oxides was possible. However each material and/or process is unique in its own way and may need to be adapted in order to make complete conversion while maintaining frustule morphology possible.

References

1. Zhou, B.L., *Bio-inspired study of structural materials.* Materials Science and Engineering C, 2000. **11**: p. 13-18.
2. Pompe W., H.W., M. Epple, W. Friess, M. Gelinsky, P. Greil, U. Hempel, D. Scharnweber, K. Schulte, *Functionally graded materials for biomedical applications.* Materials Science and Engineering, 2003. **A362**: p. 40-60.
3. Li Li, Q.-S.W.a.Y.-P.D., *Living bio-membrane bi-template route for simultaneous synthesis of lead selenide nanorods and nanotubes.* Nanotechnology, 2004. **15**: p. 1877-1881.
4. Gordon, R., *Beyond micromachining: the potential of diatoms.* TIBTECH, 1999. **17**: p. 190-196.
5. *Diatoms: Ever Wonder?* Earthquide [cited 2004 8/5]; Available from: http://www.earthguide.ucsd.edu/diatom/d1.html.
6. http://people.ccmr.cornell.edu/~uli/Pages/org-inorgmatls.html. [cited.
7. Hildebrand, M., *Biological processing of nanostructured silica in diatoms.* Progress in Organic Coatings, 2003. **47**: p. 256-266.
8. Armbrust, E.V., *Identification of a New Gene Family Expressed during the Onset of Sexual Reproduction in the Centric Diatom.* Applied and Environmental Microbiology, 1999: p. 3121-3128.
9. Hildebrand, M., *Prospects of Manipulating Diatom Silica Nanostructure.* Journal of Nanoscience and Nanotehcnology, 2005. **5**: p. 146-157.
10. Armbrust, E.V.B., John A.; Bowler, Chris; Green, Beverley R.; Martinez, Diego; Putnam, Nicholas H.; Zhou, Shiguo; Allen, Andrew E.; Apt, Kirk E.; Bechner, Michael; Brzezinski, Mark A.; Chaal, Balbir K.; Chiovitti, Anthony; Davis, Aubrey K.; Demarest, Mark S.; Detter, J. Chris; Glavina, Tijana; Goodstein, David; Hadi, Masood Z.; Hellsten, Uffe; Hildebrand, Mark; Jenkins, Bethany D.; Jurka, Jerzy; Kapitonov, Vladimir V.; Kroeger, Nils; Lau, Winnie W. Y.; Lane, Todd W.; Larimer, Frank W.; Lippmeier, J. Casey; Lucas, Susan; Medina, Monica; Montsant, Anton; Obornik, Miroslav; Parker, Micaela Schnitzler; Palenik, Brian; Pazour, Gregory J.; Richardson, Paul M.; Rynearson, Tatiana A.; Saito, Mak A.; Schwartz, David C.; Thamatrakoln, Kimberlee; Valentin, Klaus; Vardi, Assaf; Wilkerson, Frances P.; Rokhsar, Daniel S., *The genome of the diatom Thalassiosira pseudonana: Ecology, evolution, and metabolism.* Science, 2004. **306**(5693): p. 79-86.
11. Sohn H.Y, J.S., J.W.E., *Gas-Solid Reactions.* 1976, London: Academic Press, Inc. Ltd. 395.
12. Xu C., J.T., Norio Miura and Noboru Yamazoe, *Grain Size effects on gas sensitivity of porous SnO2-based elements.* Sensors and Actuators B, 1991. **3**: p. 147-155.

13. Brailsford A.D., E.M.L., *Selected aspects of gas sensing.* Sensors and Actuators B, 1998. **52**: p. 195-203.
14. Egashire, Y.S. M., *Basic Aspects and Challenges of Semiconductor Gas Sensors.* MRS Bulletin, 1999. **24**(6): p. 19-24.
15. Sun, K.S.P., H.T., *Ceramic Semiconductors for Gas Detection.* Key Engineering Materials, 1996. **115**: p. 181-190.
16. Egashira, M., *Synthesis of mesoporous TiO_2-based powders and there gas-sensing properties.* Sensors and Actuators B, 2002. **87**: p. 122-129.
17. Rumyantseva M.N., G. A.M., *Nature of Gas Sensitivity in Nanocrystalline Metal Oxides.* Russian Journal of Applied Chemistry, 2001. **74**(3): p. 440-444.
18. Sharma Rajnish K. G.L.. Sharma, M.C.B., *Effect of Nb metal ion in TiO_2 oxygen gas sensor.* Applied Surface Science, 1995. **92**: p. 647-650.
19. Rusiz A. M., G.D., J. Arbiol, A. Cornet and Joan R. Morante, *Insights into the structural and Chemical Modiffications of Nb Additive on TiO_2 Nanoparticles.* Chem. Mater., 2003. **16**(5): p. 862-871.
20. Ruiz, A., *Study of the influence of Nb content and sintering temperature on TiO_2 sensing films.* Thin Solid Films, 2003. **436**: p. 90-94.
21. Kohli, A.W., C. C.; Akbar, S. A., *Niobium pentoxide as a lean-range oxygen sensor.* Sensors and Actuators, B: Chemical, 1999. **B56(1-2)**: p. 121-128.
22. Yu-De-Wang, L.-F.Y., Zhen-Lai Zhou, Yan-Feng Li, Xing-Hui Wu, *Effects of calcining temperature on lattice constants and gas-sensing properties of Nb2O5.* Materials Letters, 2001. **49**: p. 277-281.
23. Franco J., G.S., *Ferroelectric crystals*. 1993, New York: Dover Publications, Inc. 402.
24. Shackelford, J.F., *Materials Science for Engineers*. 5th ed, ed. M. Horton. 200, Upper Saddle River, NJ: Prentice Hall. 877.
25. Kyohiko M., A.K., Kiyoshi Sakaue, Isao Takahashi, Hikaru Terauchi and Syuichi Doi, *Effects of BaTiO3 overlayers deposited on SrTiO3 on its 105K phase transition.* Surface and Interface Analysis, 2005. **37**: p. 145-148.
26. Mao Y., S.B., Sranislaus S. Wong, *Hydrothermal synthesis of perovskite nanotubes.* Chemical Communication, 2003: p. 408-409.
27. Helmenstine, A.M. *Types of Inorganic Chemical Reactions*. 2004 [cited; Available from: http://chemistry.about.com/cs/generalchemistry/a/aa072103a.htm.
28. Breslin, M.C., *Processing, microstructure, and properties of co-continuous alumina aluminum composites.* Materials Science & Engineering A, 1995. **195**: p. 113-119.
29. Wagner, F., *Interpenetrating Al_2O_3-$TiAl_3$ Alloys Produced by Reactive Infiltration.* Journal of the European Ceramic Society, 1999. **19**: p. 2449-2453.
30. Binnewies, M., *The Unusual Formation of Iron Silicide by Reaction of Iron with $SiCl_4$.* Angew.Chem. Int. Ed., 2001. **40**(19): p. 3688-3690.
31. Sandhage, K.H., *Novel, Bioclastic Route to Self-Assembled, 3D, Chemically Tailored Meso/Nanostructures: Shape-Preserving Reactive Conversion of Biosilica (diatom) Microshells.* Advanced Materials, 2002. **14**(6): p. 429-433.
32. Kalem, T., *Bio-Templated Nano-Scale Smart Materials*, in *Materials Science and Engineering*. 2004, Iowa State University: Ames. p. 34.

33. Sandhage, K.H., *Anatase assemblies from algae:coupling biological self-assembly of 3-D nanoparticle structures with synthetic reaction chemistry.* Chem. Commun., 2004: p. 796-797.
34. Rotter G. L., C.-h.C., Shu-hong Liu, Clayton Jeffryes, Jun Jiao, and James A. Hedberg, *Biosynthesis of Silicon-Germanium Oxide Nanocomposities by the Marine Diatom Nitzschia frustulum.* Journal of Nanoscience and Nanotechnology, 2005. **5**: p. 41-49.
35. Roach, J., *Nanotech Gadgets to be built by Algae?* National Geographic News, 2005.
36. Rotter, G.L.C., Chih-hug, Jeffryes, Clayton; Liu,shu-hong; Gutu, Timothy; Jiao, Jun. *Cellular biosynthesis of nanostructed semiconductor materials.* in *229th ACS National Meeting*. 2005. San Diego, CA: American Chemical Society.
37. Katsube, H.N. M., *Preparation of BaTiO3 thin films using glycolate Precursor.* Journal of Solid State Chemistry, 1997(131): p. 43-48.
38. M. Z. -C. Hu, G.A.M., E.A. Payzant, C.J. Rawn, *Homogeneous (co)precipitation of inorganic salts for synthesis of monodispersed barium titanate particles.* Journal of Materials Science, 2000. **35**: p. 2927-2936.
39. Kun-Yuan C., a.Y.-W.C., *Preparation of barium titanate ultrafine particles from rutile titania by a hydrothermal conversion.* Powder Technology, 2004. **141**: p. 69-74.
40. Hertl, W., *Kinetics of Barium Titanate Synthesis.* Journal of American Ceramic Society, 1988. **71**(10): p. 879-83.
41. Vivekanandan, T.R.N.K.R., *Precipiatiaon of Rutile and Anatase (TiO_2) Fine Powders and Their Conversion to MTiO3 (M= Ba, Sr, Ca) by the Hydrothermal Method.* Materials Chemistry and Physics, 1988. **19**: p. 533-546.
42. Shandhage K. H., M.B.D., Philip M. Huseman, Michael A. Caranna, Heremy D. Clifton, Tracia A. Bull, Timothy J. Heibel, Warren R. Overton, and Monica E. A. Schoenwaelder, *Novel, Bioclastic Route to Self-Assembled, #D, Chemically Tailored Meso/Nanostructures: Shape-Preserving Reactive Conversion of Biosilica(Diatom) Microshells.* Advanced Materials, 2002. **14**(6): p. 429-433.
43. Unocie R. R., F.M.Z., Peter M. Sarosi, Ye Cai and Kenneth H. Shandhage, *Anatase asseblies from algae: coupling biological self-assembly of 3-D nanoparticles structures with synthetic reaction chemistry.* Chemistry Communication, 2004: p. 796-797.
44. Kalem T., M.A., *Bio-Templated Nano-structured Materials*, in *Materials Science & Engineering*. 2004, Iowa State University: Ames. p. 44.
45. Riley, A.K.J.P., Marine biology, 1979. **55**: p. 29-35.
46. Begg B. D., E.R.V., and Janusz Nowotny, *Effect of Particle Size on the Room-Temperature Crystal Structure of Barium Titanate.* Journal of the American Ceramic Society, 1994. **77**(12): p. 3186-3192.
47. Vivekanandan R., T.R.N.K., *Characterization of Barium Titanate fine Powders formed from hydrothermal crystallization.* Powder Technology, 1989. **57**(3): p. 181-192.
48. Padture N. P., X.W., *Hydrothermal Synthesis of Thin Films of Barium Titanate Ceramic Nano-Tubes at 200C.* Journal of American Ceramic Society, 2003. **86**(12): p. 2215-17.

49. E. Brzozowski, a.M.S.C., *Lowering the synthesis themperature of high-purity BaTiO3 powders by modifications in the processing conditions.* Thermochimica Acta, 2002. **398**: p. 123-129.
50. D.Sarkar, J.B.a., *Formation of BaTiO3 from Barium Oxalate and TiO2.* Journal of Electroceramics, 2003. **11**: p. 131-137.
51. Faff P., G., *BaTiO3 Preparation by Reaction of TiO_2 with Ba(OH)2.* Journal of the European Ceramic Society, 1991. **8**: p. 35-39.
52. Masaru Yoshinaka, K.H., and Osamu Yamaguchi, *Formation and Sintering of TiO2(Anatase) Solid Solution in the system TiO2-SiO2.* Journal of the American Ceramic Society, 1997. **80**(10): p. 2749-53.
53. Changlong C., X.J., Dairong Chen, Yuting Zhao, *Effects of precursors on hydrothermally synthesized SrTiO3 Powders.* Materials Research Bulletin, 2001. **36**: p. 2119-2126.
54. Dudley S., M.A., *BaTiO3 Conversion*, in *Material Science Engineering*. 2005, Iowa State University: Ames.
55. Rossa J. R. H., R.H.H.S.a.K.S., *The use of niobia in oxidation catalysis.* Catalysis Today, 1993. **16**(3): p. 503-511.
56. Ziolek, I.N.M., *Niobium Compounds: Preparation, Characterization, and Application in Heterogeneous Catalysis.* Chemical Review, 1999. **99**: p. 3603-3624.
57. Nieder-Vahrenholz, H.G.S., Harald., *Oxide fluorides of niobium and tantalum.* Zeitschrift fuer Anorganische und Allgemeine Chemie, 1987. **544**: p. 122-6.
58. Hiroshi Mizoguchi, M.O., and Masahiro Hirano, *NbO2F: An oxyfluoride phase with wide band gap and electrochromic properties.* Applied Physics Letters, 2002. **80**(25): p. 4732-4734.
59. Anderson S., A.A., *The Thermal Decomposition of NbO2F.* Acta Chemica Scandinavica, 1965. **19**: p. 2136-2138.

Appendix

In order to get a reasonable understanding of how different variables affect the degree of completion, a semi quantitative method based on comparison of the peak intensities of the product-to-reactant of the most intense XRD peaks was used. A calibration curve was constructed by taking high purity powders of $BaTiO_3$ and $SrTiO_3$ and mixing with high purity titania powders in known molar ratios. The results are presented in Figure 1 and 2.

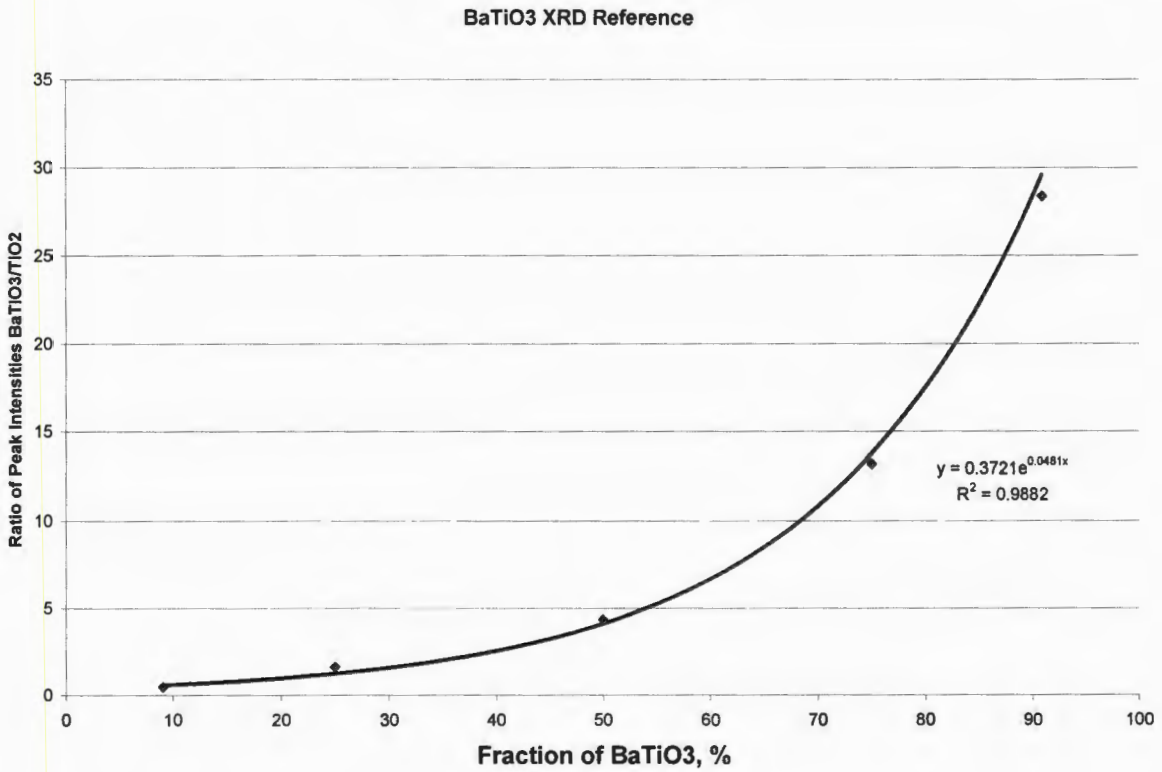

Figure 1 Calibration curve for relative XRD peak intensity ratio of $BaTiO_3$ and TiO_2 as a function of $BaTiO_3$ content.

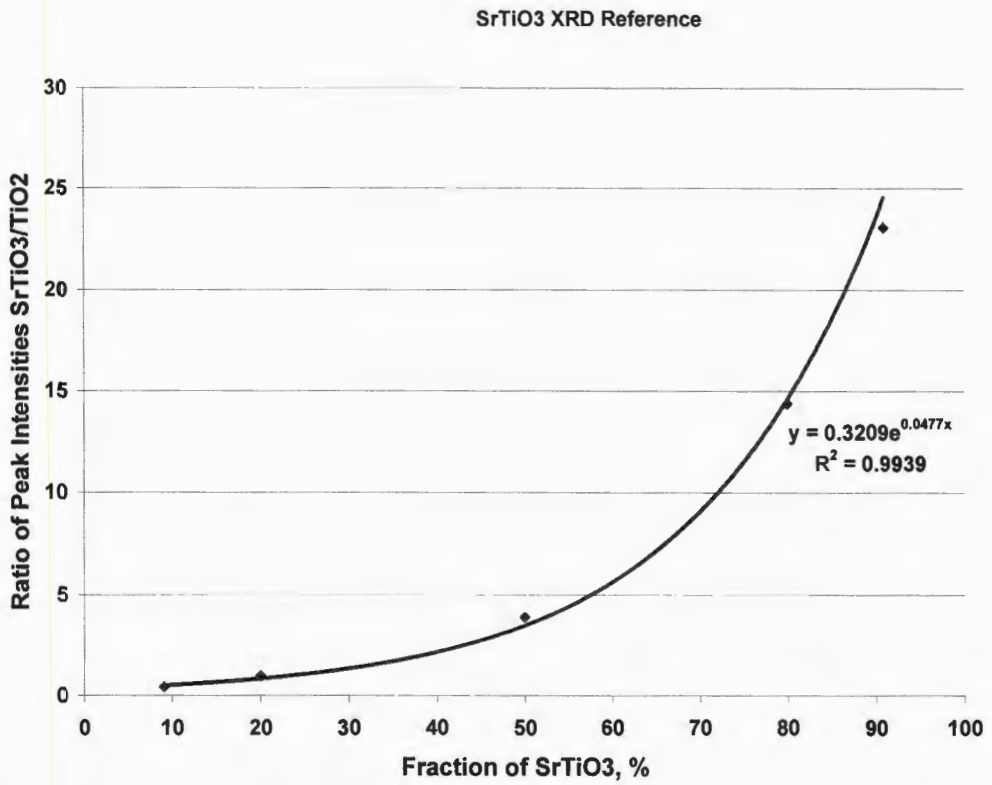

Figure 2 Calibration curve for relative XRD peak intensity ratio of $SrTiO_3$ and TiO_2 as a function of $SrTiO_3$ content.

In Figure 1 and 2, the exponential relationship between the ratio peak intensity and the molar ratio is displayed. By examining the data it can be seen that as the percent conversion decreases the peak intensity ratio falls further away from the trend line. This gives reason to believe that the accuracy of this equation may decrease as the percent conversion decreases. However, since these equations were most often utilized in the higher conversion levels, the error should be minimum. Using the calibration curves, an example of the percent conversion as a function of excess water used in reaction is given in Figure 3 for $SrTiO_3$ case.

The excess water (lower $Sr(OH)_2$ concentration) was found to increase the conversion of the $SrTiO_3$ reaction.

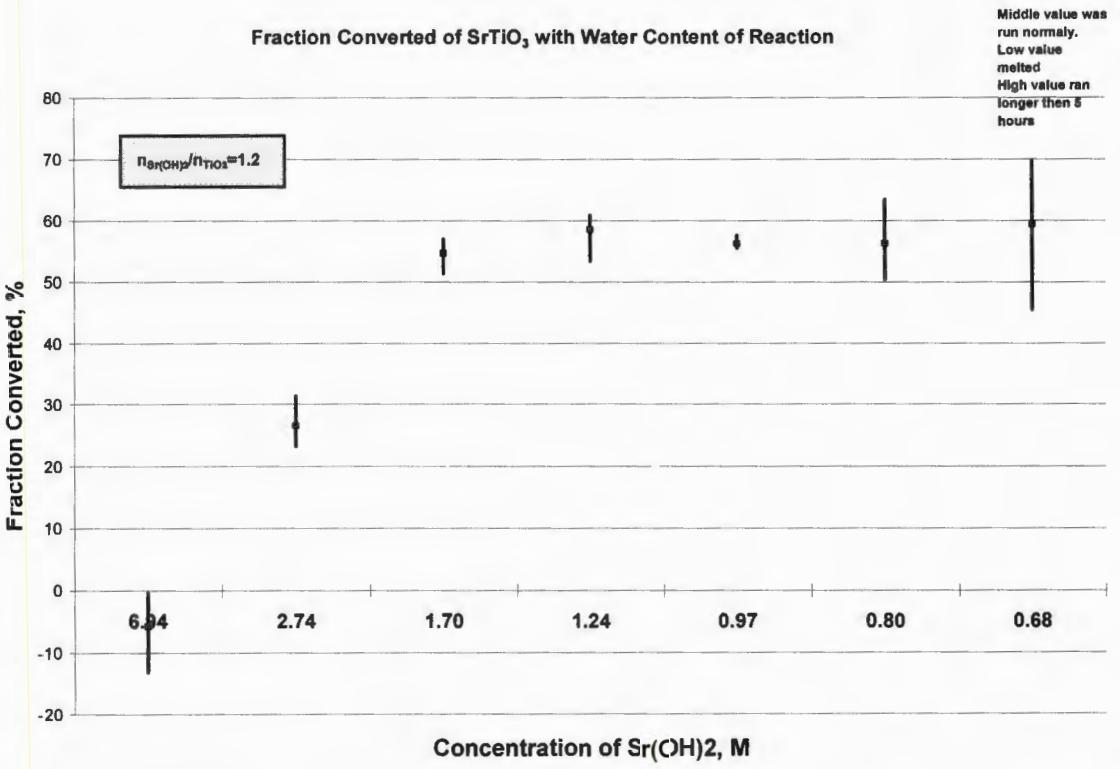

Figure 3 Degree of conversion of TiO_2 to $SrTiO_3$ as a function of [$Sr(OH)_2$]. All samples underwent the same time at temperature except for the lowest molarity of 0.68 in which a furnace error caused the highest conversion to stay at soak temperature significantly longer than 5 hours which was time at soak temperature for all other samples. The lowest value in which the jar holding the sample melted allowing the water to boil out.

Although there is some scatter in the data, it appears that $Sr(OH)_2$ concentration between 1.70 M and 0.68 M will produce approximately the same conversion when time and temperature of the reactions are constant. As seen in the case of 6.94 M where the only water is from the crystal water from $Sr(OH)_28H_2O$, there was very little conversion. This experiment also drew curiosity into the effects of excess water on $BaTiO_3$ conversion. As a result, the same type of experiments carried out and the results are displayed in Figure 4.

Experiments showed that although significant improvement of conversion is achieved by adding water to the $SrTiO_3$ reaction, the highest conversion in $BaTiO_3$ reaction is achieved with no additional water.

The relationship between time at soak temperature and percent conversion is shown in Figure 5.

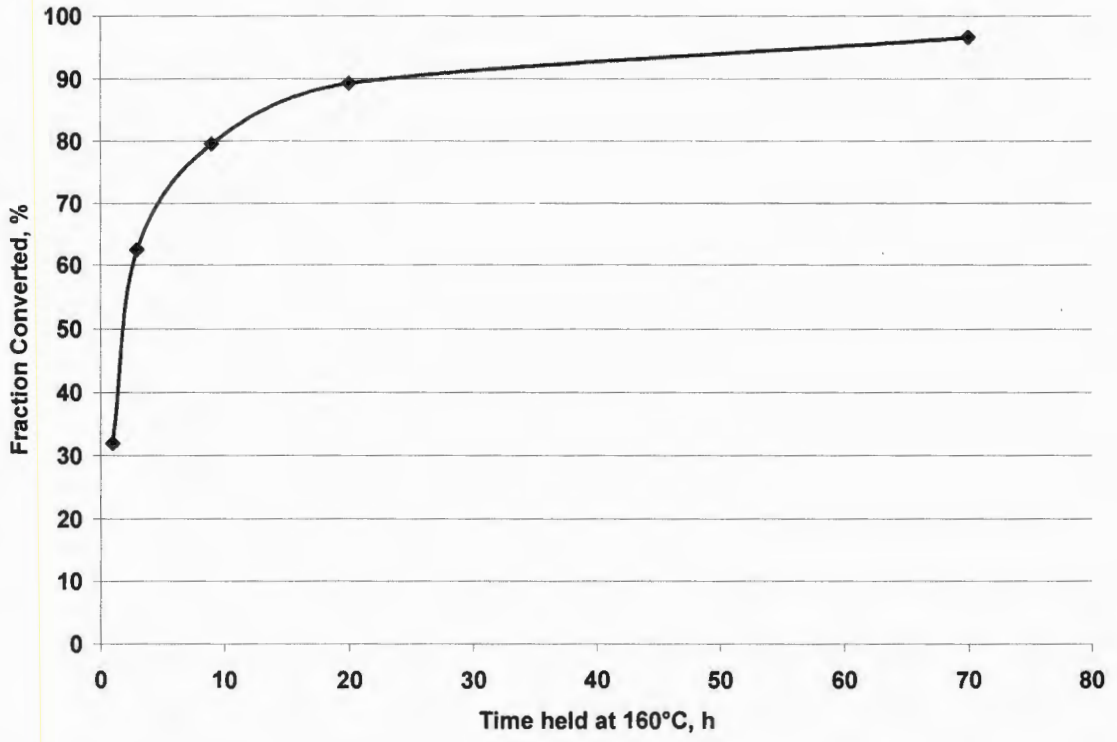

Figure 5 Degree of conversion of TiO_2 to $SrTiO_3$ as a function of time

The figure shows the excellent profile of how time affects the relationship, nearly 100% conversion was achieved at long soak times as demonstrated from the figure. One thing that has not been studied about soak time of well over 10 hours is how these soak times affect morphology of the frustules. Morphology is one of the most important requirements for these reactions, and the effects of extended soak times on these reactions have not been studied.

Different burn out times, temperatures, and atmospheres were used in order to get a single phase of Nb_2O_5. This was not achieved. Figure 6 shows how different times, temperatures and atmospheres affect the phases formed. From the diagram it can be seen that between $2\Theta = 23\text{-}28°$ lower temperature reactions show four distinct peaks which is a characteristic of oxygen-deficient phases like $NbO_{2.4}$ while higher temperature phases show three distinct peaks which is characteristic of Nb_2O_5 phases.

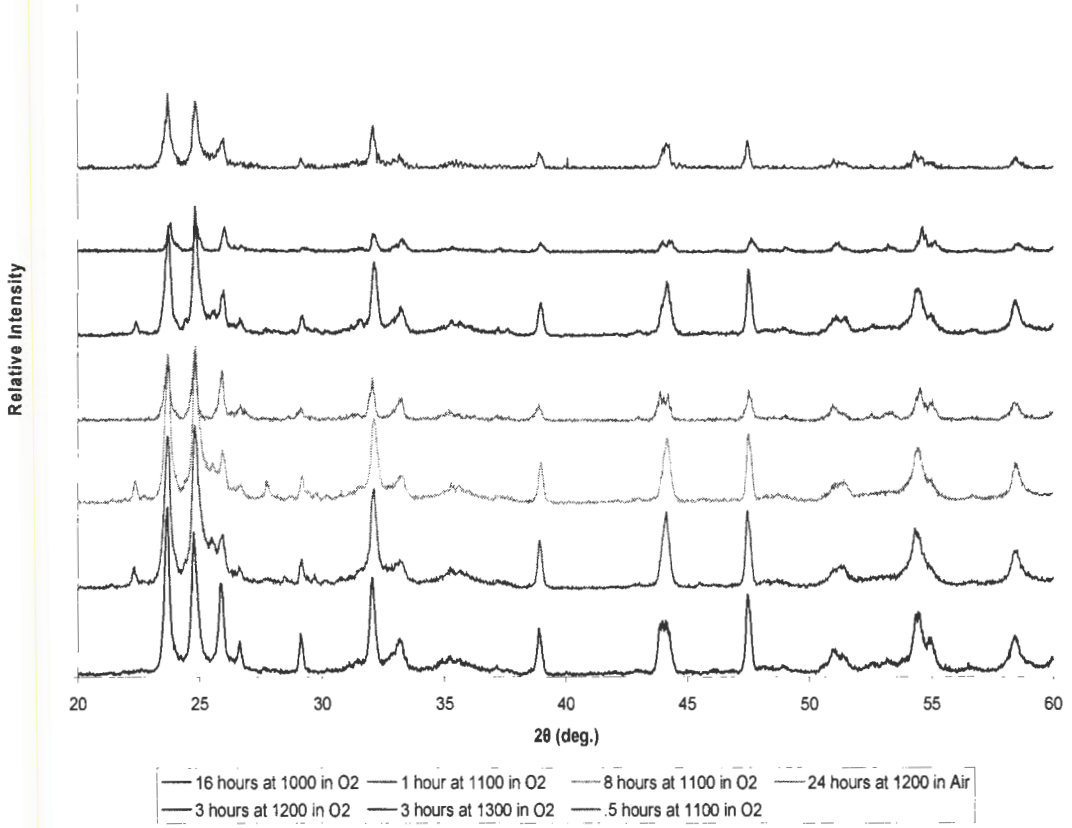

Figure 6. XRD patterns of niobium oxide formed at different heat treatment temperature and time combinations.